Research Square

Preprints are preliminary reports that have not undergone peer review.
They should not be considered conclusive, used to inform clinical practice,
or referenced by the media as validated information.

Injectable Composite hydrogel overcomes solubility-penetration-retention bottlenecks for lumbar facet joint osteoarthritis by inhibiting NLRP3 inflammasome

Yuxu Wu
First Affiliated Hospital Zhejiang University
Sicheng Huang
First Affiliated Hospital Zhejiang University
Chihao Jin
First Affiliated Hospital Zhejiang University
Junrong Lin
First Affiliated Hospital Zhejiang University
Kai Zhang
First Affiliated Hospital Zhejiang University
Qingqing Zhang
First Affiliated Hospital Zhejiang University
Yihe Hu
First Affiliated Hospital Zhejiang University
Zhiyun Feng
fengzhiyun@zju.edu.cn
First Affiliated Hospital Zhejiang University

Research Article

Keywords:

Posted Date: November 18th, 2026

DOI: https://doi.org/10.21203/rs.3.rs-11506367/v1

License: This work is licensed under a Creative Commons Attribution 4.0 International License.
Read Full License

Additional Declarations: No competing interests reported.

Injectable Composite hydrogel overcomes solubility-penetration-retention bottlenecks for lumbar facet joint osteoarthritis by inhibiting NLRP3 inflammasome

Yuxu Wu[#], MD; Sicheng Huang[#], MD; Chihao Jin[#], MD; Junrong Lin, MD; Kai Zhang, MD; Qingqing Zhang, MD; Yihe Hu*, MD; Zhiyun Feng*, MD

Department of Orthopedic Surgery, The First Affiliated Hospital, Zhejiang University School of Medicine, Hangzhou, China, 310003

*__Correspondence to__: Dr. Zhiyun Feng, 1367 Wenyi West Rd, Yuhang District, Hangzhou, Zhejiang Province, P.R.China, (311121). Email: fengzhiyun@zju.edu.cn; Dr. Yihe Hu, 1367 Wenyi West Rd, Yuhang District, Hangzhou, Zhejiang Province, P.R.China, (311121) Email: xy_huyh@163.com

Funding: This project was supported by the National Natural Science Foundation of China (No.82102599), Public Welfare Program of Science and Technology Department of Zhejiang Province (No. LTGY24H060003). The funding body played no role in the design of the study and collection, analysis, and interpretation of data.

Abstract

Lumbar facet joint osteoarthritis (FJOA) is a leading contributor to back pain, yet current administered therapies are unable to inhibit inflammatory injury of cartilage. The NLRP3 inflammasome drives the degenerative injury of cartilage by generating mature IL-1β, contributing to chondrocyte apoptosis and extracellular matrix degradation. Small-molecule NLRP3 inhibitor CY09 holds promising anti-inflammatory potential, but its poor aqueous solubility, insufficient cartilage penetration, and short intra-articular residence severely restrict intra-articular application. This study fabricated an injectable composite hydrogel (CY09@ACD/Ca-Alg) by encapsulating CY09 in cationic amino-modified β-cyclodextrin (ACD) inclusion complexes and cross-linking the complexes within a calcium-alginate network. Cy5-labelled ACD formulations showed penetration into deep layer of cartilage explants and *in vivo* fluorescence tracer revealed prolonged retention of the alginate matrix in rat facet joints up to 28 days. *In vitro*, CY09@ACD/Ca-Alg reduces NLRP3 inflammasome-associated markers, reduces mature IL-1β secretion, reduces NF-κB activation, and restores the balance between anabolic and catabolic chondrocyte phenotypes. *In vivo*, intra-articular injection of CY09@ACD/Ca-Alg reduces NLRP3 and Caspase-1 signals and local IL-1β levels, attenuates cartilage erosion, and decreases local inflammatory level. This composite hydrogel platform, combining host-guest solubilization, deep cartilage targeting, and sustained joint retention, provides a potential approach for FJOA.

Introduction

Back pain affects up to two-thirds of the population throughout their lifetime, rendering it a prominent cause of work-related disability [1,2]. Disc degeneration has historically been regarded a primary contributor to back pain, but population-based studies have reported associations between degenerative MRI findings and back pain, although these findings do not fully explain symptoms [3,4]. This inconsistent association has prompted increasing attention to alternative pain generators within the lumbar spine. Lumbar facet-joint osteoarthritis (FJOA) is currently recognized as a frequent source of back pain, and its incidence and clinical burden are substantially underestimated [5-7]. The facet joints (FJs), composed of articular cartilage, synovium, and fibrous articular capsule, represent the only true synovial joints within the spine. Clinically, patients with severe FJOA frequently exhibit spinal stenosis, presenting with radicular symptoms or neurogenic claudication. Nevertheless, current clinical treatments remain limited to temporary symptomatic relief and cannot halt progressive FJOA deterioration.

Mounting evidence indicates that inflammatory responses occupy a central position in FJOA pathogenesis, driving synovial hyperplasia, cartilage breakdown, and pain hypersensitivity. Among inflammatory mediators, Interleukin-1β (IL-1β) acts as a dominant driver of these catabolic and nociceptive processes [8-10]. IL-1β amplifies chondrocyte inflammation by upregulating prostaglandin E2 (PGE2), tumour necrosis factor-α (TNF-α) and Interleukin-6 (IL-6) in cartilage tissues, thereby triggering chondrocyte apoptosis. Meanwhile, IL-1β induces expression of matrix

metalloproteinases and aggrecanases, accelerating extracellular matrix (ECM) degradation. Maturation and secretion of bioactive IL-1β depend on the NLR pyrin domain-containing 3 (NLRP3) inflammasome, a cytosolic multi-protein complex that activates Caspase-1 to cleave pro-IL-1β [11]. Importantly, IL-1β exerts feed-forward stimulation on NLRP3 by enhancing both priming and assembly, creating a self-amplifying vicious cycle [12,13]. This amplification distinguishes the NLRP3/IL-1β axis from canonical inflammatory pathways and partially explains why FJOA progression can become self-sustaining. Accordingly, interrupting NLRP3 activation represents a rational therapeutic strategy for FJOA.

CY09 is a small-molecule inhibitor with high selectivity for NLRP3 that directly binds to the motif of NLRP3 NACHT domain, inhibiting ATPase activity, thereby abolishing inflammasome assembly and activation [14]. Cumulative pre-clinical studies have demonstrated that CY09 exerts protective therapeutic effects across a broad spectrum of NLRP3-driven inflammatory pathologies [14-16]. Notably, existing chondrocyte-focused studies confirm that CY09 inhibits NLRP3-mediated inflammation and preserves ECM homeostasis under inflammatory stimulation [15]. Nevertheless, CY09 is highly lipophilic and nearly insoluble in aqueous solutions, which prevents preparation of injectable aqueous formulations for intra-articular administration.

Although nanocarrier systems have been broadly explored for delivering drugs via intra-articular administration, most reported systems suffer from unsatisfactory cartilage-penetrating performance and short intra-articular residence time, which

greatly limits their clinical translation [17-19]. To overcome these bottlenecks, cationic nanocarriers have attracted growing research interest, as they establish electrostatic interactions with negatively-charged glycosaminoglycans (GAGs), the major anionic constituents within cartilage ECM [20-22]. In the present study, we adopt amino-modified cationic β-cyclodextrin (ACD)-based inclusion complexes to deliver CY09 (CY09@ACD). The hydrophobic interior of ACD accommodates lipophilic CY09, while its hydrophilic exterior enhances the apparent aqueous solubility and colloidal stability of the payload [23]. Furthermore, the cationic surface of ACD promotes deep cartilage penetration. When incorporated into injectable Ca-Alg hydrogel, the composite platform enables sustained CY09@ACD release, maintaining prolonged NLRP3 inhibition within the joints. This strategy provides a targeted, locally administered approach to attenuate inflammation and slow cartilage destruction in FJOA.

Herein, we designed a hydrogel platform consisting of Ca-Alg hydrogel and ACD loaded with CY09 (CY09@ACD/Ca-Alg) to ameliorate FJOA. This system simultaneously addresses the poor aqueous solubility of CY09, weak cartilage-penetrating capacity, and short intra-articular residence associated with conventional nanocarriers. Our results demonstrate that this system effectively maintains chondrocyte anabolic homeostasis in association with reduced NLRP3 inflammasome-related inflammatory markers, thereby slowing degenerative FJOA progression. This study provides a reference for designing biomaterials and supports further preclinical evaluation for FJOA treatment.

Materials and Methods

Sample Collection and Grading

Human lumbar FJ specimens were prospectively collected from June 2025 to December 2025. Degenerative FJ tissues were harvested from patients subjected to transforaminal lumbar interbody fusion. Given the unavailability of completely normal FJ specimens from living patients, minimally degenerative FJ tissues were harvested from patients with lumbar vertebral fractures and spinal cord injury to serve as low-grade control samples. Consistent inclusion criteria were applied to all enrolled patients: (1) eligibility for intraoperative FJ osteotomy; (2) no history of prior spinal surgery or lumbar infectious diseases; (3) complete preoperative lumbar CT and MRI data. This study was approved by the Ethics Committee of the First Affiliated Hospital, Zhejiang University School of Medicine (Ethics Approval Number: 2025B-0362), and written informed consent was acquired from all participants prior to sample collection.

Preoperative lumbar FJ degeneration severity was graded via the Weishaupt scoring system based on CT and MRI images [24]. A total of 43 lumbar FJ specimens were enrolled in this study, including 8 Grade 0, 12 Grade 1, 15 Grade 2, and 8 Grade 3 samples. Patient characteristics are summarized in Table S1.

Histological Evaluation

All 43 lumbar FJ specimens were immersed in 4% paraformaldehyde for fixation, then subjected to decalcification in 10% ethylenediaminetetraacetic acid (EDTA)

solution for approximately four weeks. After routine paraffin embedding, continuous 5 μm sagittal sections were prepared for histological staining. Sections were collected starting from the medial joint margin at an interval of 200 μm. Hematoxylin–eosin (H&E) staining was carried out to evaluate inflammatory-cell infiltration and osseous structural damage. Safranin-O/fast-green (SO) staining was utilized to visualize cartilage proteoglycan loss and evaluate matrix degeneration. The Osteoarthritis Research Society International (OARSI) histopathological scoring criteria were applied to quantify the overall severity of lumbar FJ cartilage degeneration [25].

Primary Chondrocyte Isolation

Primary chondrocytes were isolated from macroscopically intact lumbar FJ cartilage tissues harvested from patients with spinal cord injury during surgical decompression. Superficial intact cartilage tissues were sterilely dissected with a surgical scalpel in a laminar-flow bench. After digestion of cartilage specimens with 0.2% type II collagenase at 37°C, a 200-mesh stainless-steel filter was used to strain the cell suspension and remove undigested tissue debris. Chondrocytes were isolated and subsequently seeded in culture flasks at a density of 1×10^5 cells/cm^2 and cultured in high-glucose Dulbecco's modified Eagle medium (DMEM, Gibco, USA) supplemented with 10 % fetal bovine serum (FBS, Gibco, NY, USA) and 1 % penicillin-streptomycin double antibiotics (Gibco, USA) in a 37 °C incubator with 5 % CO_2. The culture medium was refreshed every 48 h. When cultures reached 80% confluence, cells were subcultured, and chondrocytes at passages 2–3 were used for all subsequent in vitro experiments.

For inflammatory model construction, chondrocytes were serum-starved for 24 h to synchronize cell status, then stimulated with various concentrations of IL-1β (Novoprotein, China) to induce inflammatory injury. After 12 h, 24 h and 48 h of continuous stimulation, chondrocytes were collected for Western blotting and cellular immunofluorescence detection.

Cell Viability Assay

Cytotoxicity of IL-1β and CY09 (MCE, USA) toward primary chondrocytes was determined via the Cell Counting Kit-8 (CCK-8, MCE, USA). Chondrocytes were inoculated into 96-well plates at a density of 5000 cells per well, followed by overnight culture to permit adherence. Chondrocytes were then treated with a gradient of IL-1β concentrations (0, 0.1, 1, 5, 10, 20, 50 ng/mL) and a gradient of CY09 concentrations (0, 0.1, 1, 5, 10, 20, 50 μM) for 48 h. Upon completion of treatment, medium was aspirated and cells were carefully rinsed using phosphate-buffered saline (PBS). Thereafter, 100 μL of fresh medium with 10% CCK-8 working solution was added per well, after which incubation proceeded at 37°C for 2 h. Measurements of absorbance at 450 nm were obtained using a Thermo Scientific Multiskan FC microplate reader (Thermo Fisher, USA) for determination of relative cell viability.

Western Blot Analysis

Extraction of total cellular protein was carried out using radioimmunoprecipitation assay lysis buffer (MCE, USA) supplemented with 1 mM phenylmethanesulfonyl fluoride to suppress protein degradation. Quantification of protein was carried out

using a bicinchoninic acid (BCA) protein assay kit (Beyotime, China). Each sample contributed 40 μg of protein, which was resolved on sodium dodecyl sulfate–polyacrylamide gel electrophoresis (SDS-PAGE) and electrophoretically transferred onto polyvinylidene fluoride membranes (Bio-Rad, USA). Membranes were blocked for 90 min at room temperature and subsequently incubated overnight at 4°C with primary antibodies against β-actin, NLRP3, Caspase-1, IL-1β, Caspase-3, Bax, Bcl-2, COL2, SOX9, MMP-3, MMP-13, IκBα, P65 and GAPDH. The next day, the corresponding secondary antibodies were applied to the membranes for 1 h at room temperature, and three tris-buffered saline containing Tween-20 (TBST) washes were then performed. Visualization of protein bands was achieved with an enhanced chemiluminescence (ECL) ultrasensitive detection kit (Biosharp, China) and a Chemi-Doc XRS+ imaging system (Bio-Rad, USA). Relative protein expression was subsequently analyzed quantitatively using ImageJ software.

Cellular Immunofluorescence Staining

Culture of chondrocytes was initiated in 20 mm glass-bottom confocal dishes until 80% confluence was attained. After completion of the respective treatments, three washes with PBS were performed, followed by fixation for 15 min at room temperature using 4% paraformaldehyde. Three additional PBS rinses preceded a 5-min permeabilization step with 0.3% Triton X-100, after which a 1-h block with 5% bovine serum albumin (BSA) was introduced to prevent nonspecific antibody binding. Cells were subsequently incubated overnight at 4°C with primary antibodies against NLRP3, Caspase-1, COL2, MMP-13 and P65. Cells were washed with PBS and then

incubated for 1 h at room temperature in the dark using Alexa Fluor 488- or Alexa Fluor 546-conjugated secondary antibodies. Actin was visualized with phalloidin, and nuclear counterstaining was achieved with 4′,6-diamidino-2-phenylindole (DAPI). Immunofluorescence images were randomly captured using a Leica SP8 confocal microscope (Leica, Germany) with consistent laser intensity and exposure parameters across all groups.

TUNEL Staining

Chondrocyte apoptosis was detected using the *in-situ* Cell Death Detection Kit (Beyotime, China). Briefly, treated chondrocytes were subjected to fixation with 4% paraformaldehyde for 15 min, followed by a PBS rinse. TUNEL staining was performed strictly in accordance with the manufacturer's instructions. Fluorescence images were randomly acquired via confocal microscopy, and TUNEL fluorescence was quantified as mean fluorescence intensity for each group, as reported in Figures 2 and 5.

Synthesis of CY09@Amino-Modified β-Cyclodextrin (CY09@ACD) Complex

Calcium chloride dihydrate (≥99 %), sodium alginate (≥98 %), and 6-monodeoxy-6-monoamino-β-cyclodextrin (ACD, ≥98 %) were purchased from Yuanye Biotechnology (Shanghai, China). The CY09@ACD host-guest supramolecular complex was synthesized based on previously established protocols [26,27]. In brief, 20 μL of CY09 stock solution (10 mg/mL in DMSO) was slowly drop-wise added into 2 mL of aqueous ACD solution (0.27 mg/mL) under continuous

vigorous magnetic stirring. The mixture was reacted for 24 h at room temperature, followed by freeze-drying to obtain crude CY09@ACD powder. To eliminate unencapsulated free CY09, the lyophilized material was redissolved in deionized water, followed by repeated centrifugation (10000 rpm, 20 min, three cycles). The final supernatant containing purified CY09@ACD complex was collected. Interactions between ACD and CY09 were assessed via UV-vis absorption spectroscopy.

Fabrication of Injectable CY09@ACD/Ca-Alg Composite Hydrogel

To screen the optimal cross-linking formulation, blank calcium-alginate (Ca-Alg) hydrogels with gradient cross-linking densities were prepared. Equal volumes of sodium alginate solution (15 mg/mL) and $CaCl_2$ aqueous solution (1, 2, 4 mg/mL) were mixed under continuous stirring. Combined with syringe injectability evaluation and rheological modulus detection, the formulation containing 15 mg/mL sodium alginate and 2 mg/mL $CaCl_2$ was considered the most favorable system for the subsequent composite hydrogel preparation. For CY09-loaded composite hydrogel fabrication, 0.74 mg of purified CY09@ACD complex was pre-dissolved in 1 mL of 15 mg/mL sodium alginate solution, which was then uniformly mixed with 1 mL of 2 mg/mL $CaCl_2$ solution via continuous stirring to form homogeneous CY09@ACD/Ca-Alg hydrogel networks.

Physicochemical Characterization of Hydrogels

The rheological properties (storage modulus G′, loss modulus G″) of blank Ca-Alg

and CY09@ACD/Ca-Alg hydrogels were measured using a Kinexus ultra+ rotational rheometer (Malvern, UK) under constant oscillatory conditions (0.1 Pa shear stress, 1 Hz frequency). Chemical structural changes of different materials were characterized by Fourier-transform infrared spectroscopy (FT-IR, Nicolet iS20, Thermo Scientific, USA). The microscopic morphology of hydrogels was observed via scanning electron microscopy (ZEISS Sigma 300, Germany), and elemental composition was analyzed by X-ray photoelectron spectroscopy (K-Alpha, Thermo Scientific, USA).

In vitro CY09 Release Profile Detection

Dialysis bags (molecular weight cutoff = 8000 Da) loaded with CY09@ACD/Ca-Alg hydrogel (containing 0.37 mg encapsulated CY09@ACD) and 1 mL of pH 6.8 PBS were immersed in 30 mL of PBS release medium. Free CY09@ACD solution was set as the control group. Incubation of the whole system proceeded in a constant-temperature shaker at 37°C and 60 rpm. At predetermined time points, samples (1 mL each) of the release medium were withdrawn, with an equal volume of fresh PBS being replenished to maintain a constant system volume. Measurement of absorbance at 350 nm was carried out for the collected samples using a UV-vis spectrophotometer, from which the cumulative in vitro release percentage of CY09 was calculated.

Cellular Uptake, *Ex-Vivo* Cartilage Penetration, and *in vivo* Joint Retention Assay

For cellular uptake detection, primary chondrocytes were seeded in 30 mm glass-bottom confocal dishes at a density of 1×10^5 cells per dish and cultured for 48 h for stable adherence. ACD and Ca-Alg were respectively labeled with Sulfo-Cy5 NHS ester (Lumiprobe, Hunt Valley, USA) to prepare Cy5-tagged ACD (Cy5-ACD) and Cy5-Ca-Alg fluorescent probes. Chondrocytes were co-incubated with different probes for 3 h. Following incubation, medium removal was followed by three PBS washes to clear uninternalized probes. Fixation of the treated chondrocytes was then performed for 15 min with 4% paraformaldehyde, and a final PBS rinse was applied. Actin was labeled with phalloidin, cell nuclei were stained with DAPI, and intracellular probe distribution was visualized via fluorescence microscopy.

For *ex-vivo* cartilage penetration evaluation, fresh porcine knee articular cartilage was trimmed into uniform cylindrical explants (8 mm diameter, 4 mm height, 1.5 mm thickness). Cartilage explants were incubated with free Cy5, Cy5-Ca-Alg, Cy5-ACD, or Cy5-ACD@Ca-Alg solution for 12 h, 36 h, and 72 h, respectively. After incubation, the explants were fully rinsed with PBS and cut into 80 μm-thick continuous sections using a vibratome. A confocal laser scanning microscope (Leica SP8, Leica, Germany) was used to observe and quantify fluorescence distribution and intensity, after which ImageJ software was employed for statistical analysis.

The retention time of the hydrogel was measured by injecting free Cy5, Cy5-Ca-Alg, Cy5-ACD, or Cy5-ACD@Ca-Alg into the facet joint of the rats. After injecting 10 μL into the facet joint, the fluorescence was detected using the IVIS-spectrum system (BIOSPACE LAB) at excitation wavelength of 675 nm and emission wavelength of

694 nm. Images were obtained at days 1, 3, 7, 14, 21, and 28. When fluorescence intensity could not be detected, the rats were euthanized and knee joints and major organs (heart,liver, spleen, and kidney) were collected. The images in each time point were repeated in triplicates.

Live-Dead Cell Fluorescence Staining

Chondrocytes were inoculated into 24-well plates at a density of 1×10^5 cells per well and allowed to grow for 24 h to approximately 80% confluence. Thereafter, the cells were assigned to different experimental groups and treated accordingly. Once treatment was complete, the culture medium was discarded and the cells were rinsed twice with sterile PBS. A Calcein-AM/PI Live/Dead Cell Staining Kit (Beyotime, China) was used to evaluate cell viability. The working solution—composed of 2 μM Calcein-AM and 4 μM propidium iodide (PI) in PBS—was prepared, and 300 μL was dispensed into each well. After 15–20 min of incubation at 37°C in the dark, fluorescence images were captured without delay using laser scanning confocal microscopy. Three random visual fields were imaged per group, and the live/dead cell ratio was quantified using ImageJ software.

Transwell Migration Assay

The migratory ability of chondrocytes was measured using Transwell chambers fitted with 8 μm-pore polycarbonate membranes (NEST Biotechnology, China). Chondrocytes were serum-starved for at least 12 h to synchronize the cell cycle, then digested and re-suspended in serum-free DMEM. The upper chamber received 2×10^4

cells in 200 μL of serum-free medium, and 500 μL of complete medium containing 10% FBS—supplemented with the corresponding experimental treatments—was placed in the lower chamber to act as a chemoattractant. After 24 h of incubation at 37°C with 5% CO_2, non-migrated cells remaining on the upper surface of the membrane were carefully wiped off using sterile cotton swabs. Cells that had migrated to the lower membrane were fixed for 20 min with 4% paraformaldehyde and subsequently stained for 25 min with 0.1% crystal violet solution at room temperature. Following thorough rinsing and natural drying, photomicrographs were taken and the number of migrated cells was counted with ImageJ.

ELISA

An in vitro and in vivo assessment of the inflammatory response was carried out by measuring IL-1β, TNF-α, IL-6, PGE_2, and IL-8 levels in cell culture supernatants and facet joint tissue homogenates using ELISA kits (Shanghai Hengyuan Biological Technology, China). Thereafter, the obtained concentrations were derived from the respective standard curves.

Transcriptome Sequencing

6-well plates were seeded with chondrocytes and used for their culture. After the cells had grown to 80% confluence, stimulation was carried out by adding IL-1β for 24 h. Three replicate samples then received CY09@ACD/Ca-Alg. The culture was sustained for three days, and TRIzol reagent was used to extract total RNA. Assessment of RNA quality, library construction, sequencing, and bioinformatic

analysis were all performed by Servicebio, China

FJOA Model Establishment and *in vivo* Intervention

All procedures involving animals were reviewed and approved by the Institutional Animal Care and Use Committee of the First Affiliated Hospital, Zhejiang University School of Medicine (Permit Number: 2024-K001), conforming to institutional guidelines for laboratory animal care. Eight-week-old male Sprague-Dawley (SD) rats were purchased from the Zhejiang Provincial Laboratory Animal Center, and random assignment was performed to distribute them into five groups.

The lumbar FJOA model was established via spinal destabilization surgery as previously reported [28,29]. Briefly, pentobarbital sodium (35 mg/kg) was administered intraperitoneally to anesthetize the rats. Under sterile conditions, an incision was made along the posterior midline, after which the paraspinal muscles were separated by blunt dissection to expose the L4–L5 vertebral spinous processes. The facet joints were progressively degenerated through complete resection of the spinous processes, supraspinous ligaments, and interspinous ligaments. At 2 and 4 weeks post-operatively, rats in each group were injected intra-articularly with 10 μL of vehicle, free CY09, blank ACD/Ca-Alg hydrogel, or CY09@ACD/Ca-Alg composite hydrogel, respectively. The rats were kept in a warm, quiet environment with standard feed and drinking water. Post-operative analgesia was achieved by administering buprenorphine (0.05 mg/kg) via subcutaneous injection once daily for three times. All rats were euthanized 8 weeks post-operatively, and lumbar FJ tissues

were harvested for histological, immunohistochemical and immunofluorescence analyses.

Histological Staining for Rat Tissue

Harvested rat FJ tissues were immersed in 4% paraformaldehyde for 24 h to allow fixation, after which they were decalcified in EDTA-NaOH solution on a horizontal shaker for four weeks. After routine dehydration, paraffin embedding, and 5 μm-thick transverse sectioning, tissue sections were prepared for staining.

For H&E staining, rehydrated sections were stained with hematoxylin for 5 min at room temperature, rinsed with distilled water, subjected to differentiation with 1% hydrochloric acid in 70% ethanol, blued in running tap water, and counter-stained with 0.5% eosin for 1 min. Dehydration was then carried out through 95% and absolute ethanol, followed by clearing with xylene and mounting in neutral resin. Nuclei were stained blue–purple, while the cytoplasm and extracellular matrix exhibited a pink-to-red color.

For Safranin-O staining, rehydrated sections were stained with 0.1 % Safranin-O working solution for 15 min at room temperature, rapidly rinsed with distilled water, differentiated with 95 % ethanol, fully dehydrated with absolute ethanol, cleared with xylene, and mounted. Glycosaminoglycan-rich cartilage matrix was stained bright red.

For toluidine blue staining, sections were placed in 1% toluidine blue working solution (pH 2.3) and stained for 20 min at room temperature. Distilled water was used to rinse off the excess dye, and dilute acetic acid was employed for light

differentiation as needed. The sections were then dehydrated, cleared, and mounted for observation.

All stained sections were observed and imaged using an Olympus microscope equipped with an image-acquisition system (Nikon, Japan). Three random visual fields (400× magnification) were captured per section, and positive staining intensity was quantified and averaged for statistical analysis.

Immunohistochemical Staining

Dewaxing and rehydration of paraffin sections were followed by two 15-min PBS washes. A 15-min incubation with 3% H_2O_2 was used to block endogenous peroxidase activity. Antigen retrieval was performed by heating the sections in boiling citrate buffer (pH 6.0) for 10 min. The sections were then blocked with 5% BSA for 20 min at room temperature and incubated overnight at 4°C with primary antibodies against Aggrecan and COL2. The subsequent day, anti-rabbit secondary antibodies were applied to the sections for 1 h at room temperature. A diaminobenzidine (DAB) chromogenic kit served to visualize target protein expression. After counter-staining with hematoxylin, the sections were dehydrated using gradient ethanol, cleared in xylene, and mounted with neutral resin for microscopic observation and quantitative analysis.

Tissue Immunofluorescence Staining

To detect the in vivo expression of MMP-13, NLRP3, and Caspase-1 in rat lumbar FJ cartilage, tissue immunofluorescence staining was carried out. Briefly, dewaxed

sections were subjected to heat-mediated antigen retrieval using citrate buffer (pH 6.0) and then cooled naturally to room temperature. After permeabilization with 0.3% Triton X-100 for 10 min, a 30 min incubation with 5% BSA was applied to block nonspecific binding sites. Overnight incubation of the sections with primary antibodies at 4°C was followed by three PBS washes; the sections were then treated with fluorophore-conjugated secondary antibodies for 1 h in the dark at room temperature. Counter-staining of cell nuclei was performed with DAPI for 5 min, and the slides were mounted in anti-fade mounting medium. A confocal microscope was employed to acquire all fluorescence images using identical exposure parameters, enabling comparison between groups.

Statistical Analysis

All experimental data are presented as mean ± standard deviation (SD). Quantitative data differences among multiple groups were analyzed by one-way analysis of variance (ANOVA) followed by Tukey's post-hoc test. Non-parametric data were analyzed using the Kruskal-Wallis H test. All statistical analyses were performed using STATA 12.0 software (StataCorp LP, TX, USA). A p value < 0.05 was defined as statistically significant.

Results

Clinically-relevant facet joint degeneration correlates with elevated NLRP3 inflammasome activation

To characterize the molecular pathological features of FJOA, graded degenerative facet-joint tissues (Grade 0-3) were analyzed by CT, MRI, and histological staining. Progressive structural destruction, cartilage erosion and subchondral bone remodeling could be clearly observed from Grade 0 to Grade 3 on CT and MRI scans (**Figure 1A-B**). Safranin-O and H&E staining further confirmed stepwise loss of proteoglycan, disorganized chondrocyte distribution and gradual cartilage degradation along with increased pathological grade (**Figure 1C-D**). Immunohistochemical staining revealed that the positive proportions of NLRP3, Caspase-1 and IL-1β were markedly increased as degeneration worsened (**Figure 1E-H**). Quantitative statistics demonstrated significantly higher percentages of $NLRP3^+$, $Caspase\text{-}1^+$ and $IL\text{-}1\beta^+$ chondrocytes in higher-grade FJOA specimens. The data obtained indicate a positive correlation between NLRP3 inflammasome-related marker expression and the cross-sectional severity of facet-joint degeneration, providing a pathological rationale for targeting NLRP3 to alleviate FJOA. Patient characteristics are summarized in **Table S1**.

Validation of CY09 cytoprotective effects in primary chondrocytes via blocking the activation of NLRP3 inflammasome

An IL-1β-stimulated chondrocyte inflammatory injury model was established to

mimic the FJOA inflammatory microenvironment. Cell viability assays illustrated dose-dependent cytotoxicity of IL-1β toward chondrocytes at concentrations higher than 10 ng/mL (**Figure 2A**). As the standard stimulation protocol for subsequent experiments, IL-1β at 10 ng/mL was applied for 24 h. Moreover, Western-blot analysis showed that IL-1β provoked robust up-regulation of NLRP3 in a dose- and time-dependent manner (**Figure 2B-E**).

The cytotoxic profile of CY09 was then assessed; CY09 exhibited negligible toxicity below 5 μM, while obvious cell damage occurred above 10 μM (**Figure 2F**). Therefore, 5 μM CY09 was selected for subsequent *in vitro* functional assays. Western-blot results verified that CY09 treatment effectively suppressed the over-activation of NLRP3, Caspase-1 and IL-1β triggered by IL-1β (**Figure 2G-H**). Immunofluorescence staining further demonstrated that CY09 distinctly reduced NLRP3 protein abundance (**Figure 2I-K**). Then TUNEL staining confirmed that CY09 mitigated IL-1β-induced chondrocyte apoptosis in association with reduced NLRP3 expression (**Figure 2J-L**). Moreover, cartilage-matrix-associated immunofluorescence indicated that CY09 rescued COL2 loss and inhibited excessive MMP-13 accumulation under inflammatory stress (**Figure 2M-N**). Collectively, CY09 could inhibit NLRP3 inflammasome activation, restrain inflammatory cell apoptosis and maintain extracellular matrix homeostasis in inflamed chondrocytes.

Fabrication and physicochemical characterization of injectable CY09@ACD/Ca-Alg composite hydrogel

To achieve intra-articular, deep-cartilage delivery of CY09, injectable calcium-alginate composite hydrogel incorporating amino-modified β-cyclodextrin-drug complexes (CY09@ACD/Ca-Alg) was constructed. Ca-Alg hydrogels with tunable cross-linking density were prepared by varying $CaCl_2$ concentrations (1, 2, 4 mg/mL) to identify optimal injectable formulation. At 1 mg/mL $CaCl_2$, the precursor remained sol-like with extremely low storage modulus (G′). The 2 mg/mL $CaCl_2$ group achieved favorable sol-gel transition, proper G′ magnitude and good syringe injectability. In contrast, 4 mg/mL $CaCl_2$ yielded overly rigid hydrogel with poor extrudability (**Figure 3A, B**). Consequently, 2 mg/mL $CaCl_2$ was adopted for composite hydrogel fabrication. CY09@ACD supramolecular complexes were mixed with alginate precursor and cross-linked *in-situ* by Ca^{2+} to produce CY09@ACD/Ca-Alg hydrogel (**Figure 3C**). Rheological measurements revealed that loading CY09@ACD barely altered G′ and loss modulus (G″) compared with blank Ca-Alg hydrogel; both groups displayed pronounced shear-thinning properties, supporting satisfactory injectable performance (**Figure 3D-E**). Scanning electron microscopy revealed a porous and compact microstructure in the composite alginate matrix. Energy-dispersive X-ray spectroscopy (EDX) elemental mapping visualized uniform distribution of characteristic F (CY09) and N (ACD) signals throughout the scaffold, verifying homogeneous dispersion of drug-carrier complexes (**Figure 3F**). Fourier-transform infrared (FT-IR) spectra exhibited characteristic absorption peaks originating from CY09 aromatic C-H vibration and ACD pyranose C-O-C stretching in CY09@ACD/Ca-Alg samples. X-ray photoelectron spectroscopy (XPS) further

detected Ca 2p signals associated with calcium cross-linking, together with F 1s, S 2p and N 1s signals associated with the incorporated drug and carrier. Combined FT-IR and XPS results confirmed successful integration of CY09@ACD into the alginate polymeric network (**Figure 3G-M**). The UV-Vis absorption spectra reveal that CY09@ACD displays an obvious shift of the absorption peak compared with free CY09, consistent with interactions between CY09 and amino-cyclodextrin (**Figure 3N**). *In vitro* release profiles demonstrated sustained CY09 release from CY09@ACD/Ca-Alg hydrogel over 144 h (**Figure 3O**).

***In vitro* cellular uptake, *ex-vivo* cartilage-penetrating, and *in vivo* joint retention performance of ACD-based delivery system**

To characterize cellular internalization and tissue penetration capability, Cy5 fluorescent dye was conjugated onto ACD and Ca-Alg to trace the labelled carrier formulations. Confocal laser-scanning microscopy revealed that free Cy5 exhibited minimal intracellular fluorescence signal in chondrocytes, and Cy5-Ca-Alg only achieved weak cellular uptake. By comparison, Cy5-ACD and Cy5-ACD@Ca-Alg groups presented prominent intracellular red fluorescence, proving that cationic ACD greatly facilitated chondrocyte internalization (**Figure 4A, C**). *Ex-vivo* porcine cartilage explant model was applied to evaluate deep-tissue penetration behaviour at 12 h, 36 h and 72 h. Free Cy5 and Cy5-Ca-Alg were predominantly restricted to the superficial cartilage layer with scarce inward diffusion. Cy5-ACD achieved moderate penetration, whereas Cy5-ACD@Ca-Alg exhibited robust, time-dependent deep-cartilage fluorescence signal. Quantitative mean-fluorescence-intensity analysis

demonstrated higher intratissue tracer abundance in the Cy5-ACD@Ca-Alg group than in the free Cy5 and Cy5-Ca-Alg groups across the three time points (**Figure 4B, 4D-F**).

We then performed *in vivo* fluorescence imaging to monitor the local retention of formulations within lumbar facet joints over 28 days (**Figure 4G**). Free Cy5 was rapidly cleared from the injection site within 3 days. The Cy5-ACD group displayed moderate retention, with fluorescence largely disappearing by day 7. However, both Cy5-Ca-Alg and Cy5-ACD@Ca-Alg groups showed prolonged local residence, with retained strong fluorescence signals at the facet joint region up to day 28. Quantitative radiant efficiency analysis confirmed that the composite hydrogel significantly extended the intra-articular residence time of ACD carriers (**Figure 4H**). Collectively, these results demonstrate that the injectable Cy5-ACD@Ca-Alg hydrogel can efficiently deliver ACD carriers into chondrocytes and porcine cartilage explants, while achieving long-term local retention in the facet joint cavity.

CY09@ACD/Ca-Alg hydrogel alleviates chondrocyte apoptosis and restores chondrocyte ECM homeostasis via suppressing NLRP3 inflammasome

Next, we systematically compared the protective effects of free CY09, blank ACD/Ca-Alg and CY09@ACD/Ca-Alg hydrogel on IL-1β-injured chondrocytes. Both Live-Dead staining and CCK-8 assay demonstrated that CY09@ACD/Ca-Alg markedly improved chondrocyte viability under inflammatory challenge (**Figure 5A-B**). Western-blot results showed that CY09@ACD/Ca-Alg more effectively

down-regulated NLRP3, Caspase-1 and IL-1β protein abundance than other groups (**Figure 5C-F**). Immunofluorescence staining for NLRP3 and Caspase-1 further validated the strongest inhibitory effect on inflammasome activation in the CY09@ACD/Ca-Alg group (**Figure 5G-H**). Apoptosis-related protein detection illustrated that CY09@ACD/Ca-Alg reduced pro-apoptotic Caspase-3 and Bax expression while elevating anti-apoptotic Bcl-2 (**Figure 5I-L**). Consistent with these observations, intervention with CY09@ACD/Ca-Alg led to a marked reduction in inflammatory cell apoptosis, as shown by TUNEL staining (**Figure 5M-N**).

We further evaluated restoration of chondrogenic phenotype. Toluidine-blue and Alcian-blue staining showed enhanced glycosaminoglycan deposition in the CY09@ACD/Ca-Alg group (**Figure 6A**). Transwell migration assays demonstrated that CY09@ACD/Ca-Alg rescued migration defects of inflamed chondrocytes **(Figure 6B, D)**. Western-blot and immunofluorescence analyses showed that CY09@ACD/Ca-Alg significantly up-regulated COL2 and SOX9, while repressing catabolic MMP-3 and MMP-13 (**Figure 6C, 6E-J**). ELISA measurements of cell-culture supernatants indicated that CY09@ACD/Ca-Alg substantially decreased secretion of multiple pro-inflammatory mediators including IL-1β, IL-6, TNF-α, IL-8 and PGE2 (**Figure 6K-O**). Collectively, the composite hydrogel elicits comprehensive chondro-protective bioactivity: suppressing NLRP3-driven inflammation, reducing pro-inflammatory cytokine release, restraining cell apoptosis, improving chondrocyte migration and restoring the anabolic cartilage phenotype.

Transcriptomic Profiling and Protein Analysis Show Reduced NF-κB Signaling

To decipher global transcriptional changes induced by CY09@ACD/Ca-Alg, RNA sequencing was conducted on IL-1β-stimulated chondrocytes treated with or without the composite hydrogel. Gene-expression signatures that differed markedly between the two cohorts were revealed by hierarchical-clustering heatmaps (**Figure 7A**). The volcano plot illustrated large numbers of differentially expressed genes (DEGs), with both up-regulated and down-regulated genes after CY09@ACD/Ca-Alg exposure (**Figure 7B**). Enrichment analysis based on the Gene Ontology (GO) framework indicated that the enriched terms included DNA replication, cell-cycle processes, chromosome-associated components, and molecular binding functions (**Figure 7C**). Kyoto Encyclopedia of Genes and Genomes (KEGG) pathway bubble plots highlighted NF-κB signaling among the most significantly perturbed pathways (**Figure 7D**). Gene-set-enrichment analysis (GSEA) further confirmed significant negative enrichment of NF-κB-associated gene signatures (**Figure 7E**). To validate transcriptomic predictions, NF-κB-axis protein markers were examined by western blot. Phosphorylation of IκBα and P65 triggered by IL-1β was reduced after CY09@ACD/Ca-Alg treatment (**Figure 7F**). Immunofluorescence demonstrated that IL-1β-induced P65 nuclear translocation was largely abrogated by CY09@ACD/Ca-Alg (**Figure 7G**). Of note, CY09 directly targets NLRP3 ATPase activity and does not directly interfere with NF-κB signaling; the observed NF-κB suppression may involve reduced IL-1β-mediated inflammatory feedback, although its causal relationship to NLRP3 blockade was not established in this study. These transcriptomic and biochemical data support chondroprotection associated with

attenuation of IL-1β/NF-κB/NLRP3-related inflammatory signaling.

CY09@ACD/Ca-Alg ameliorates facet-joint degeneration in the rat FJOA model

In-vivo therapeutic efficacy of CY09@ACD/Ca-Alg was evaluated using a rat lumbar facet-joint instability FJOA model. H&E, Safranin-O and toluidine-blue staining revealed severe cartilage erosion, proteoglycan loss and matrix disorganization in untreated FJOA animals. Free CY09 and blank ACD/Ca-Alg conferred partial mitigation of pathological alterations. In contrast, CY09@ACD/Ca-Alg treatment substantially preserved cartilage architecture and proteoglycan abundance (**Figure 8A-D**). Quantitative histological metrics including OARSI grade, modified Mankin score, residual cartilage thickness and relative GAG content confirmed optimal therapeutic outcomes in the CY09@ACD/Ca-Alg-treated cohort (**Figure 8E-H**). Immunohistochemical and immunofluorescence staining for cartilage-matrix biomarkers showed that CY09@ACD/Ca-Alg effectively retained COL2 and Aggrecan levels while diminishing MMP-13 abundance within facet-joint cartilage (**Figure 9A-G**). Moreover, NLRP3 and Caspase-1 positive signals were significantly reduced after CY09@ACD/Ca-Alg administration, indicating effective local suppression of NLRP3 inflammasome activation *in vivo* (**Figure 9D-E, 9H-J**). Pro-inflammatory-cytokine (IL-1β, IL-6, TNF-α) quantification in facet joint demonstrated that intra-articular CY09@ACD/Ca-Alg lowered inflammatory burden in the joints (**Figure 9K-M**). Collectively, these *in vivo* results verify that injectable CY09@ACD/Ca-Alg hydrogel retards facet joint degeneration via suppression of NLRP3 inflammasome mediated inflammatory injury.

CY09@ACD/Ca-Alg exhibits favourable *in vivo* biocompatibility

Following efficacy validation, *in vivo* biocompatibility of CY09@ACD/Ca-Alg was assessed via biochemical assays and organ histology after intra-articular injection. Examination of the principal organs (heart, liver, spleen, lung, and kidney) by H&E staining disclosed no apparent inflammatory cell infiltration or architectural abnormalities (**Figure S1**). No significant differences were detected among the groups with respect to serum biochemical parameters of hepatic and renal function (**Figure S1**). These measurements did not identify overt systemic toxicity under the tested conditions.

Discussion

Inflammatory injury is central to cartilage degeneration, and NLRP3 inflammasome activation is widely implicated in osteoarthritis pathogenesis. This study documents an association between NLRP3 inflammasome-related marker expression and human lumbar facet-joint degeneration. Conventional intra-articular therapies are hampered by rapid joint-space clearance and poor penetration into deep cartilage layers. We engineered a cationic ACD-based CY09 complex integrated within Ca-Alg injectable hydrogel. The cationic ACD component is intended to promote cartilage penetration through electrostatic attraction to anionic GAGs, while the alginate network functions as a sustained-release depot. By locally delivering CY09 to interrupt the NLRP3/IL-1β axis, this composite hydrogel attenuates chondrocyte catabolism and slows facet-joint cartilage degeneration, offering new perspectives for therapeutic design for lumbar FJOA.

Historically, disc degeneration has been considered the primary source of back pain [30,31]. Increasing clinical evidence now highlights FJOA as an important pain generator, and it is also a pivotal contributor of spinal stenosis [5-7]. Most studies have focused on disc degeneration, whereas far fewer investigations have addressed facet-joint degeneration. The pathological features of FJOA resemble knee osteoarthritis, with cartilage degeneration as an initiating event [32,33]. Pro-inflammatory cytokines are key drivers of disease onset and progression. IL-1β is robustly up-regulated in osteoarthritic joint tissues and exerts broad catabolic effects [34,35]. The NLRP3 inflammasome is critical for generating mature IL-1β, thereby

triggering downstream inflammatory injury and cartilage-matrix breakdown [34,35]. In the present study, using IL-1β-stimulated chondrocyte model, we confirmed that IL-1β can also promote the activation of NLRP3 inflammasome, driving chondrocyte apoptosis and ECM degradation. These observations provide a rationale for testing whether pharmacological NLRP3 blockade can halt facet-joint cartilage degeneration.

Intra-articular drug delivery represents an attractive strategy to maximize local drug exposure while minimizing systemic adverse effects [17,36]. Two major bottlenecks persist for anti-NLRP3 small-molecule agents: short residence within the joint cavity and insufficient penetration through dense cartilage ECM, which limits therapeutic efficacy [18,36]. Calcium-alginate hydrogels are well-established biocompatible platforms for sustained drug release of local depot, and release kinetics can be tuned by adjusting cross-linking density [37,38]. Also, calcium-ion concentration is a critical determinant for alginate mesh pore size, and subsequent cargo release profiles [39]. The in vitro release profile extended over 144 h, and Cy5-labelled carrier signals persisted locally for up to 28 days. These observations do not establish the intra-articular pharmacokinetics of CY09 or therapeutic drug concentrations after a single injection; the efficacy study used injections at 2 and 4 weeks after surgery.

β-cyclodextrin is biocompatible and widely used to improve solubility of poorly water-soluble drugs, with several FDA-approved pharmaceutical formulations based on cyclodextrin technology [40,41]. In our system, host-guest complexation with ACD attenuated the aggregation-associated spectral red-shift of free CY09, consistent with drug–carrier interactions in aqueous solution. Free small-molecule drugs are

typically confined to the cartilage surface after intra-articular injection, which is a major cause of unsatisfactory anti-inflammatory outcomes [42]. Cationic biomaterials bind electrostatically to negatively-charged cartilage ECM and facilitate deep tissue infiltration [43]. Cartilage-degeneration studies have validated cation-functionalized carriers for deep-layer cartilage delivery of anti-inflammatory and anti-oxidant payloads [44]. These precedents support our strategy combining ACD-mediated deep cartilage penetration and NLRP3-targeted immunomodulation for FJOA therapy. Cy5-labelled tracer experiments verified that cationic ACD facilitates chondrocyte uptake and deep *ex-vivo* cartilage penetration in this study.

Beyond the chondrocyte-centric response, the facet-joint synovial lining harbours resident macrophages, which constitute a major cellular source of NLRP3-dependent mature IL-1β [45,46]. Potential effects on synovial macrophages and nociceptor sensitization would be clinically relevant for FJOA-associated pain [7]. Locally injected CY09@ACD/Ca-Alg could potentially act on two joint compartments: the alginate depot releases payload into the synovial space, whereas cationic ACD drives penetration into negatively-charged cartilage matrix. Macrophage responses, synovial targeting, and pain outcomes were not measured in this study.

Transcriptomic profiling revealed that NF-κB signaling was among the most significantly altered pathways after CY09@ACD/Ca-Alg treatment. Prior literature reports that NLRP3 can be regulated by Smad, p38, NF-κB and MAP-kinase cascades [47,48]. Previous work demonstrated that IL-1β promotes NLRP3 transcription via NF-κB in nucleus pulposus and endothelial-cell senescence models [12,13].

Consistently, our RNA-seq and western-blot validation showed IL-1β-driven NF-κB pathway activation in chondrocytes. It should be emphasized that CY09 exerts direct pharmacological inhibition on NLRP3 ATPase and does not directly target NF-κB signaling. The observed reduction in IκBα phosphorylation and P65 nuclear translocation is therefore not a direct drug effect. Instead, CY09 suppresses NLRP3-dependent mature IL-1β secretion, which removes autocrine IL-1β stimulation that fuels further NF-κB activation and NLRP3 transcription. Therefore, therapeutic interruption at the proximal NLRP3 node is sufficient to collapse downstream inflammatory amplification.

This study has several limitations. First, although we observe elevated NLRP3 inflammasome-related markers in degenerative human facet-joint tissues, our experimental setup cannot establish a direct causal link between NLRP3 activity and facet-joint-derived nociception. Evaluating FJOA-evoked pain behavior remains challenging both for human cohorts and rodent models. Second, the rodent FJOA model cannot fully recapitulate human-scale joint biomechanics and disease progression, future large-animal (porcine or canine) studies are required to evaluate long-term hydrogel biodegradation, local safety and therapeutic performance under human-relevant biomechanical loading. Third, our investigation focuses primarily on the NLRP3-dominant inflammatory axis; additional pathways contributing to facet-joint degeneration deserve further exploration.

In summary, this study supports the involvement of NLRP3 inflammasome-related inflammatory activity in cartilage degeneration in FJOA. To break this inflammatory

cascade, we constructed an injectable composite hydrogel CY09@ACD/Ca-Alg: amino-modified β-cyclodextrin forms host-guest inclusion complexes with CY09, which is incorporated within calcium-alginate as a local drug depot. Cy5-labelled ACD formulations show penetration into porcine cartilage explants, consistent with the design rationale of electrostatic interactions with anionic cartilage ECM components, whereas the alginate hydrogel sustains CY09 release and prolongs joint residence, thereby addressing solubility, penetration, and retention challenges for local CY09 delivery. In IL-1β-stimulated chondrocytes and a rat lumbar-facet-instability FJOA model, CY09@ACD/Ca-Alg reduces NLRP3 inflammasome-associated markers, reduces mature IL-1β secretion and reduces NF-κB signaling, thereby attenuating chondrocyte apoptosis, preventing proteoglycan depletion and limiting facet-joint cartilage erosion. These findings establish a mechanism-driven, locally-delivered therapeutic strategy to interrupt the NLRP3/IL-1β cascade in FJOA and support further preclinical evaluation of this platform for anti-inflammatory therapy for degenerative articular disorders.

References

1. Deyo RA, Weinstein JN. Low back pain. N Engl J Med. 2001; doi:10.1056/NEJM200102013440508.

2. Murray CJL. The Global Burden of Disease Study at 30 years. Nat Med. 2022; doi:10.1038/s41591-022-01990-1.

3. Videman T, Battie MC, Gibbons LE, Maravilla K, Manninen H, Kaprio J. Associations between back pain history and lumbar MRI findings. Spine (Phila Pa 1976). 2003; doi:10.1097/01.BRS.0000049905.44466.73.

4. Kjaer P, Leboeuf-Yde C, Korsholm L, Sorensen JS, Bendix T. Magnetic resonance imaging and low back pain in adults: a diagnostic imaging study of 40-year-old men and women. Spine (Phila Pa 1976). 2005; doi:10.1097/01.brs.0000162396.97739.76.

5. Gellhorn AC, Katz JN, Suri P. Osteoarthritis of the spine: the facet joints. Nat Rev Rheumatol. 2013; doi:10.1038/nrrheum.2012.199.

6. Won HS, Yang M, Kim YD. Facet joint injections for management of low back pain: a clinically focused review. Anesth Pain Med (Seoul). 2020; doi:10.17085/apm.2020.15.1.8.

7. Du R, Xu G, Bai X, Li Z. Facet joint syndrome: pathophysiology, diagnosis, and treatment. J Pain Res. 2022; doi:10.2147/jpr.S389602.

8. Berenbaum F. Osteoarthritis as an inflammatory disease (osteoarthritis is not osteoarthrosis!). Osteoarthritis Cartilage. 2013; doi:10.1016/j.joca.2012.11.012.

9. Robinson WH, Lepus CM, Wang Q, Raghu H, Mao R, Lindstrom TM, et al. Low-grade inflammation as a key mediator of the pathogenesis of osteoarthritis. Nat Rev Rheumatol. 2016; doi:10.1038/nrrheum.2016.136.

10. Chevalier X, Eymard F. Anti-IL-1 for the treatment of OA: dead or alive? Nat Rev Rheumatol. 2019; doi:10.1038/s41584-019-0185-y.

11. Kelley N, Jeltema D, Duan Y, He Y. The NLRP3 inflammasome: an overview of mechanisms of activation and regulation. Int J Mol Sci. 2019; doi:10.3390/ijms20133328.

12. Chen F, Jiang G, Liu H, Li Z, Pei Y, Wang H, et al. Melatonin alleviates intervertebral disc degeneration by disrupting the IL-1β/NF-κB-NLRP3 inflammasome positive feedback loop. Bone Res. 2020; doi:10.1038/s41413-020-0087-2.

13. Romero A, Dongil P, Valencia I, Vallejo S, San Hipólito-Luengo Á, Díaz-Araya G, et al. Pharmacological blockade of NLRP3 inflammasome/IL-1β-positive loop mitigates endothelial cell senescence and dysfunction. Aging Dis. 2022; doi:10.14336/ad.2021.0617.

14. Jiang H, He H, Chen Y, Huang W, Cheng J, Ye J, et al. Identification of a selective and direct NLRP3 inhibitor to treat inflammatory disorders. J Exp Med. 2017; doi:10.1084/jem.20171419.

15. Zhang Y, Lin Z, Chen D, He Y. CY-09 attenuates the progression of osteoarthritis via inhibiting NLRP3 inflammasome-mediated pyroptosis. Biochem Biophys Res Commun. 2021; doi:10.1016/j.bbrc.2021.03.055.

16. Tousif S, Bhati AS, Titus AS, Jaiswal A, Ansari I, Huque A, et al. Cardiomyocytes HIPK2 regulates myocardial inflammation and heart function through purinergic signaling. Cell Commun Signal. 2026; doi:10.1186/s12964-026-02919-8.

17. Kalairaj MS, Pradhan R, Saleem W, Smith MM, Gaharwar AK. Intra-articular injectable biomaterials for cartilage repair and regeneration. Adv Healthc Mater. 2024; doi:10.1002/adhm.202303794.

18. Lin J, Jia S, Cao F, Huang J, Chen J, Wang J, et al. Research progress on injectable microspheres as new strategies for the treatment of osteoarthritis through promotion of cartilage repair. Adv Funct Mater. 2024; doi:10.1002/adfm.202400585.

19. Yang F, Zhang Y, Niu X, Han G. Design strategies of biomaterial-based intra-articular drug delivery system for osteoarthritis therapy. J Control Release. 2026; doi:10.1016/j.jconrel.2025.114496.

20. Bajpayee AG, Grodzinsky AJ. Cartilage-targeting drug delivery: can electrostatic interactions help? Nat Rev Rheumatol. 2017; doi:10.1038/nrrheum.2016.210.

21. Geiger BC, Wang S, Padera RF Jr, Grodzinsky AJ, Hammond PT. Cartilage-penetrating nanocarriers improve delivery and efficacy of growth factor treatment of osteoarthritis. Sci Transl Med. 2018; doi:10.1126/scitranslmed.aat8800.

22. Wu Y, Feng Y, Hu F, Zheng X, Ding Y, Liu X, et al. Engineered stem cell clusters for extracellular vesicles-mediated gene delivery to rejuvenate chondrocytes and facilitate chondrogenesis in osteoarthritis therapy. Adv Sci (Weinh). 2025; doi:10.1002/advs.202500964.

23. Jansook P, Ogawa N, Loftsson T. Cyclodextrins: structure, physicochemical properties and pharmaceutical applications. Int J Pharm. 2018; doi:10.1016/j.ijpharm.2017.11.018.

24. Weishaupt D, Zanetti M, Boos N, Hodler J. MR imaging and CT in osteoarthritis of the lumbar facet joints. Skeletal Radiol. 1999; doi:10.1007/s002560050503.

25. Gerwin N, Bendele AM, Glasson S, Carlson CS. The OARSI histopathology initiative - recommendations for histological assessments of osteoarthritis in the rat. Osteoarthritis Cartilage. 2010; doi:10.1016/j.joca.2010.05.030.

26. Králová J, Kejik Z, Bríza T, Poucková P, Král A, Martásek P, et al. Porphyrin-cyclodextrin conjugates as a nanosystem for versatile drug delivery and multimodal cancer therapy. J Med Chem. 2010; doi:10.1021/jm9007278.

27. Pedotti S, Ginestra G, Granata G, Ferreri L, Gambera G, Petralia S, et al. Synthesis and characterization of heptakis(methylaminoethanol)-β-cyclodextrin, carvacrol complexation and evaluation of antioxidant, antibacterial and antibiofilm activities. Carbohydr Polym. 2026; doi:10.1016/j.carbpol.2025.124540.

28. Xue P, Wang S, Lyu X, Wan M, Li X, Ma L, et al. PGE2/EP4 skeleton interoception activity reduces vertebral endplate porosity and spinal pain with low-dose celecoxib. Bone Res. 2021; doi:10.1038/s41413-021-00155-z.

29. Xie Y, Liu Q, Tan J, Lu Y, Li Y, Ye H, et al. CAP-CD56+CD271+ BMSCs exos-loaded PVA/SA sustained-release hydrogel attenuates chondrocyte senescence and ameliorates lumbar facet joint osteoarthritis. Bioact Mater. 2026; doi:10.1016/j.bioactmat.2025.10.027.

30. Chou D, Samartzis D, Bellabarba C, Patel A, Luk KD, Kisser JM, et al. Degenerative magnetic resonance imaging changes in patients with chronic low back pain: a systematic review. Spine (Phila Pa 1976). 2011; doi:10.1097/BRS.0b013e31822ef700.

31. Binch ALA, Fitzgerald JC, Growney EA, Barry F. Cell-based strategies for IVD repair: clinical progress and translational obstacles. Nat Rev Rheumatol. 2021; doi:10.1038/s41584-020-00568-w.

32. Nakamura A, Rampersaud YR, Nakamura S, Sharma A, Zeng F, Rossomacha E, et al. microRNA-181a-5p antisense oligonucleotides attenuate osteoarthritis in facet and knee joints. Ann Rheum Dis. 2019; doi:10.1136/annrheumdis-2018-213629.

33. Fine N, Lively S, Séguin CA, Perruccio AV, Kapoor M, Rampersaud R. Intervertebral disc degeneration and osteoarthritis: a common molecular disease spectrum. Nat Rev Rheumatol. 2023; doi:10.1038/s41584-022-00888-z.

34. Kapoor M, Martel-Pelletier J, Lajeunesse D, Pelletier JP, Fahmi H. Role of proinflammatory cytokines in the pathophysiology of osteoarthritis. Nat Rev Rheumatol. 2011; doi:10.1038/nrrheum.2010.196.

35. Konttinen YT, Sillat T, Barreto G, Ainola M, Nordström DC. Osteoarthritis as an autoinflammatory disease caused by chondrocyte-mediated inflammatory responses. Arthritis Rheum. 2012; doi:10.1002/art.33451.

36. Evans CH, Kraus VB, Setton LA. Progress in intra-articular therapy. Nat Rev Rheumatol. 2014; doi:10.1038/nrrheum.2013.159.

37. Yang X, Li C, Yan C, Tian J, Yang H, Li S, et al. Flowerbed-inspired Mg-loaded scaffold accelerates critical-sized bone-defect repair by reprogramming the microenvironment. ACS Nano. 2026; doi:10.1021/acsnano.6c02723.

38. Xu M, Peng W, Yu G, Xiao Z, Zhao Z, Xu Z, et al. Clinically translatable injectable hydrogel platform for dual intraoperative elevation and postoperative healing in endoscopic submucosal dissection. ACS Nano. 2025; doi:10.1021/acsnano.5c14055.

39. Su CY, Li D, Wang LJ, Wang Y. Green double crosslinked starch-alginate hydrogel regulated by sustained calcium ion-gluconolactone release for human motion monitoring. Chem Eng J. 2023; doi:10.1016/j.cej.2022.140653.

40. Zhou X, Luo Z, Baidya A, Kim HJ, Wang C, Jiang X, et al. Biodegradable β-cyclodextrin conjugated gelatin methacryloyl microneedle for delivery of water-insoluble drug. Adv Healthc Mater. 2020; doi:10.1002/adhm.202000527.

41. Li G, Zhu P, Gao C, Cai Y, Feng R, Sun J, et al. Hydroxypropyl-β-cyclodextrin co-delivery hydrogel of crisaborole and curcumin for combinational antioxidant/anti-inflammatory therapy of vitiligo. Mater Today Bio. 2026; doi:10.1016/j.mtbio.2025.102728.

42. Pan Y, Peng Y, Han J, Zhang W, Xu X, Zhao M, et al. Precision targeting and regenerative therapies in articular cartilage diseases with AI-driven theranostics. J Nanobiotechnology. 2026; doi:10.1186/s12951-026-04934-w.

43. Vedadghavami A, Wagner EK, Mehta S, He T, Zhang C, Bajpayee AG. Cartilage penetrating cationic peptide carriers for applications in drug delivery to avascular negatively charged tissues. Acta Biomater. 2019; doi:10.1016/j.actbio.2018.12.004.

44. Wang W, Liu C, Sun Y. Multifunctional mPDA@Mel-AB/BG hydrogels: integrating ROS scavenging, inflammation suppression, and cartilage repair for osteoarthritis therapy. J Control Release. 2025; doi:10.1016/j.jconrel.2025.114067.

45. Bondeson J, Wainwright SD, Lauder S, Amos N, Hughes CE. The role of synovial macrophages and macrophage-produced cytokines in driving aggrecanases, matrix metalloproteinases, and other destructive and inflammatory responses in osteoarthritis. Arthritis Res Ther. 2006; doi:10.1186/ar2099.

46. Yan M, Song Z, Kou H, Shang G, Shang C, Chen X, et al. New progress in basic research of macrophages in the pathogenesis and treatment of low back pain. Front Cell Dev Biol. 2022; doi:10.3389/fcell.2022.866857.

47. Tschopp J, Schroder K. NLRP3 inflammasome activation: the convergence of multiple signalling pathways on ROS production? Nat Rev Immunol. 2010; doi:10.1038/nri2725.

48. Fann DYW, Lim YA, Cheng YL, Lok KZ, Chunduri P, Baik SH, et al. Evidence that NF-κB and MAPK signaling promotes NLRP inflammasome activation in neurons following ischemic stroke. Mol Neurobiol. 2018; doi:10.1007/s12035-017-0394-9.

Figure Legends

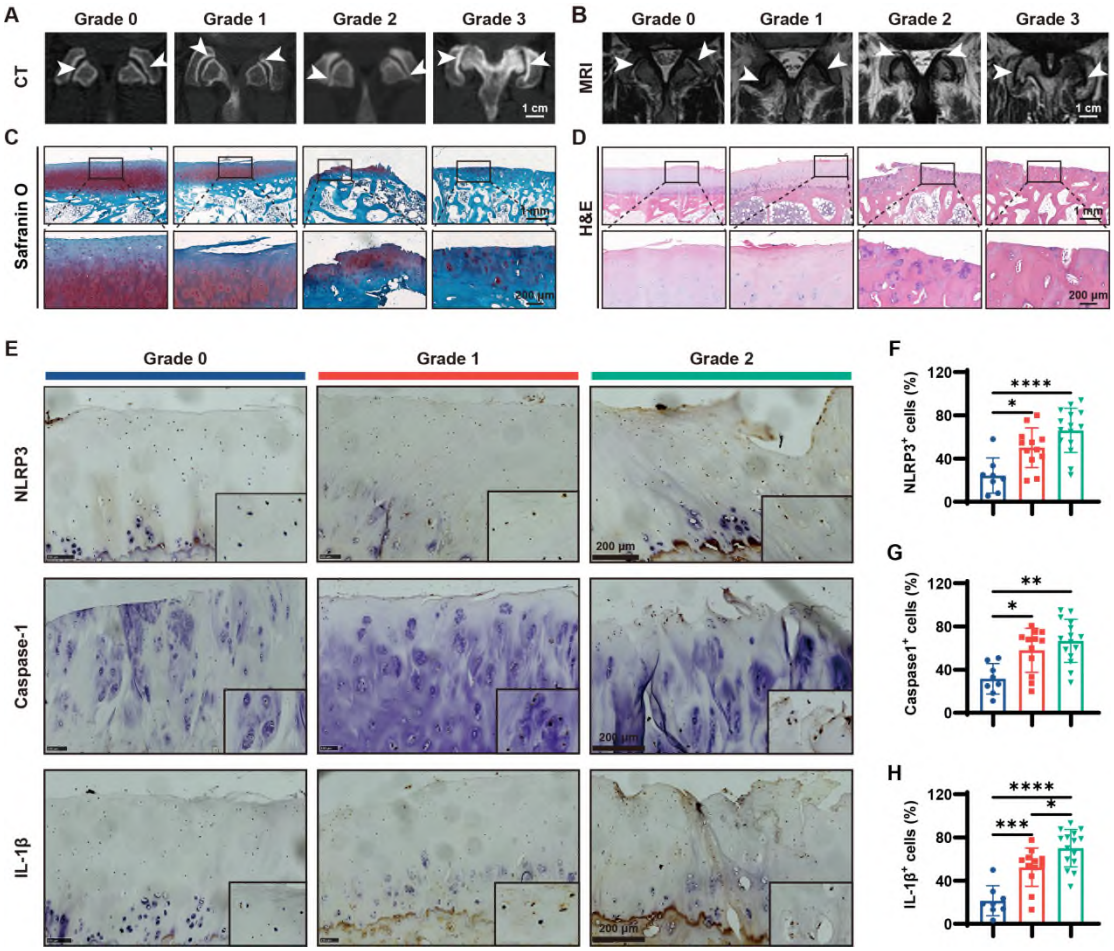


Figure 1. NLRP3 inflammasome activation positively correlates with the severity of human facet joint degeneration.

(A, B) Representative CT and MRI images of human facet joints with different degenerative grades (Grade 0-3). White arrowheads indicate facet-joint structures. Scale bar = 1 cm. (C) Safranin-O histological staining for facet-joint cartilage across Grade 0-3. Scale bars: upper = 1 mm, lower = 200 μm. (D) H&E staining showing histological alterations accompanying progressive facet-joint degeneration. Scale bars: upper = 1 mm, lower = 200 μm. (E) Immunohistochemical staining of NLRP3, caspase-1 and IL-1β in human facet-joint cartilage of Grade 0-2. Scale bar = 200 μm. (F-H) Quantitative statistics for percentages of $NLRP3^{+}$, $caspase\text{-}1^{+}$ and $IL\text{-}1\beta^{+}$ positive chondrocytes among different degenerative grades. Data are presented as

mean ± SD. *p < 0.05, **p < 0.01, ***p < 0.001, ****p < 0.0001. CT, computed tomography; MRI, magnetic resonance imaging; H&E, hematoxylin-eosin; NLRP3, NOD-like receptor pyrin domain-containing-3; IL-1β, interleukin-1β.

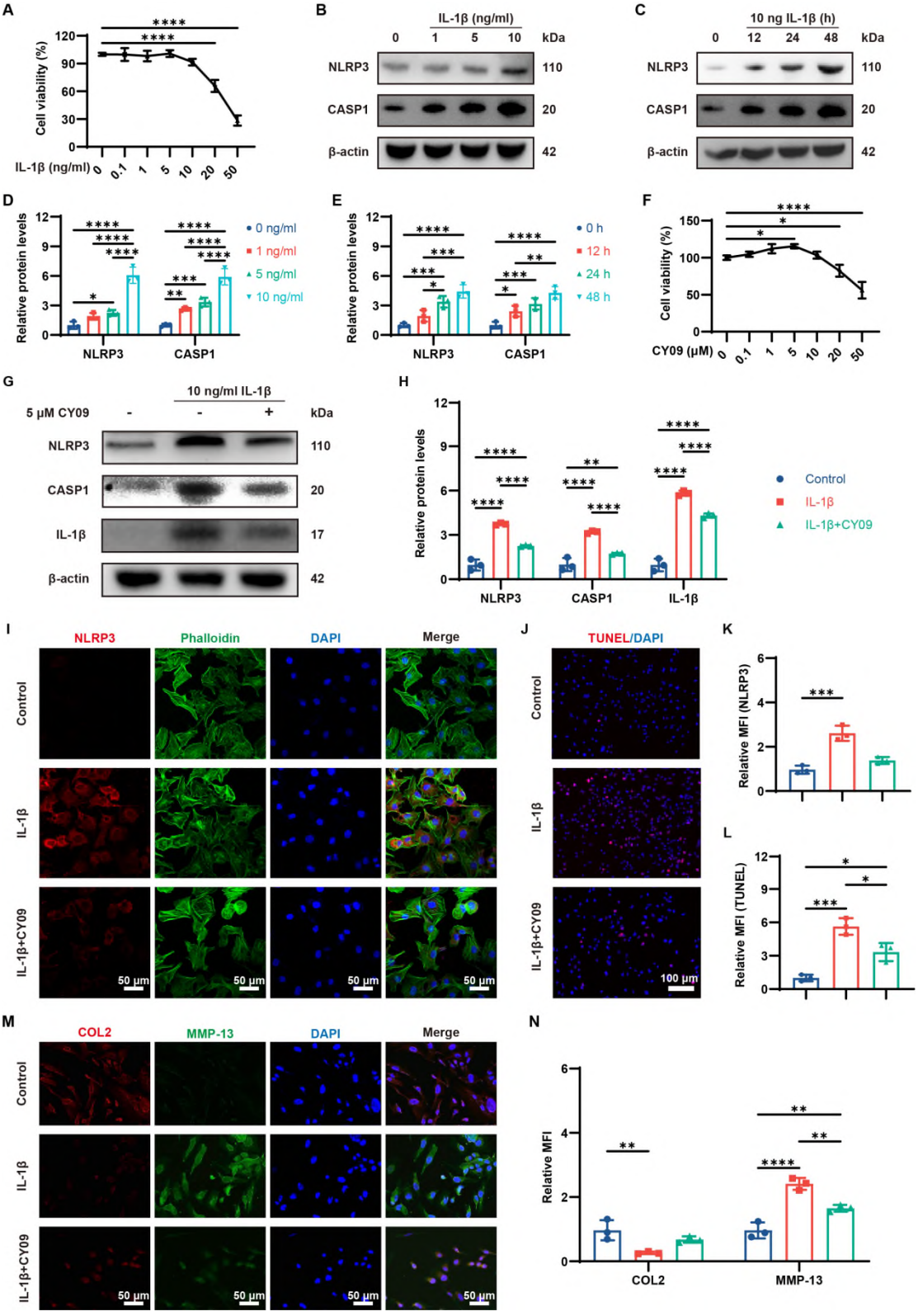


Figure 2. CY09 inhibits NLRP3 inflammasome activation and rescues chondrocytes from IL-1β-provoked inflammatory damage *in-vitro*.

(A) Cell viability of chondrocytes after incubation with gradient concentrations of IL-1β (0-50 ng/mL). (B, D) Western-blot bands and quantitative analysis of NLRP3 and caspase-1 protein expression upon stimulation with different IL-1β dosages. (C, E) Western-blot quantification demonstrating time-dependent NLRP3 inflammasome activation induced by 10 ng/mL IL-1β. (F) Cytotoxicity evaluation of CY-09 on primary chondrocytes at serial concentrations ranging from 0. 1 μM to 50 μM. (G, H) Representative western-blot images and quantitative statistics for NLRP3, caspase-1 and mature IL-1β from Control, IL-1β and IL-1β + 5 μM CY09 groups. (I, K) Immunofluorescence staining and quantitative mean-fluorescence-intensity (MFI) analysis for NLRP3 (red); F-actin was stained by phalloidin (green), nuclei were counter-stained with DAPI (blue). Scale bar = 50 μm. (J, L) TUNEL staining and corresponding MFI quantification for detecting inflammatory cell death. Scale bar = 100 μm. (M, N) Immunofluorescence of cartilage-matrix markers COL2 (red) and MMP-13 (green), together with quantitative fluorescence analysis. Scale bar = 50 μm. Data are presented as mean ± SD. *$p < 0.05$, **$p < 0.01$, ***$p < 0.001$, ****$p < 0.0001$. NLRP3, NOD-like receptor pyrin domain-containing-3; IL-1β, interleukin-1β; COL2, type-II collagen; MMP, matrix metalloproteinas; caspase-1, CASP1; MFI, mean fluorescence intensity; DAPI, 4′,6-diamidino-2-phenylindole; TUNEL, terminal deoxynucleotidyl transferase-mediated dUTP nick-end labelling.

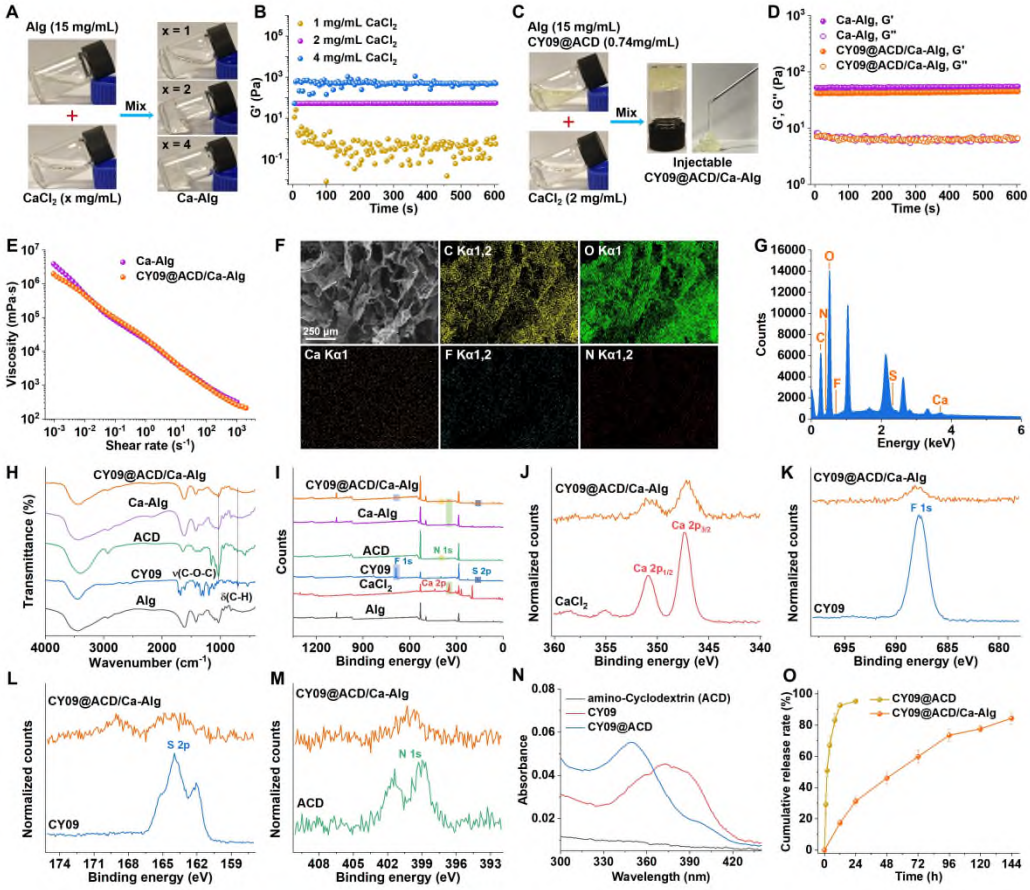


Figure 3. Characterization and performance of CY09@ACD/Ca-Alg hydrogels.

(A, C) Representative images showing the in situ formation of Ca-Alg hydrogels with varying degrees of crosslinking, as well as the CY09@ACD/Ca-Alg hydrogel. (B, D) Rheological properties of Ca-Alg and CY09@ACD/Ca-Alg hydrogels with different crosslinking degrees under constant stress (0.1 Pa) and frequency (1 Hz). (E) Viscosity curves as a function of shear rate for Ca-Alg and CY09@ACD/Ca-Alg hydrogels. (F, G) SEM image, corresponding elemental distribution mapping, and EDX profile of the CY09@ACD/Ca-Alg hydrogel. (H) FTIR spectra of the CY09@ACD/Ca-Alg hydrogel. (I) XPS survey spectra of CY09@ACD/Ca-Alg hydrogel and other control materials; (J–M) high-resolution XPS spectra of Ca 2p, F 1s, S 2p, and N 1s for CY09@ACD/Ca-Alg hydrogel compared with other materials. (N) UV-Vis spectra of CY09 and CY@ACD aqueous solution. (O) Release profiles of CY09 from CY09@ACD and CY09@ACD/Ca-Alg hydrogels. SEM, scanning

electron microscopy; EDX, energy-dispersive X-ray spectroscopy; FT-IR, Fourier-transform infrared spectroscopy; XPS, X-ray photoelectron spectroscopy; G′, storage modulus; G″, loss modulus; ACD, amino-modified β-cyclodextrin; Ca-Alg, calcium-alginate; Alg, alginate.

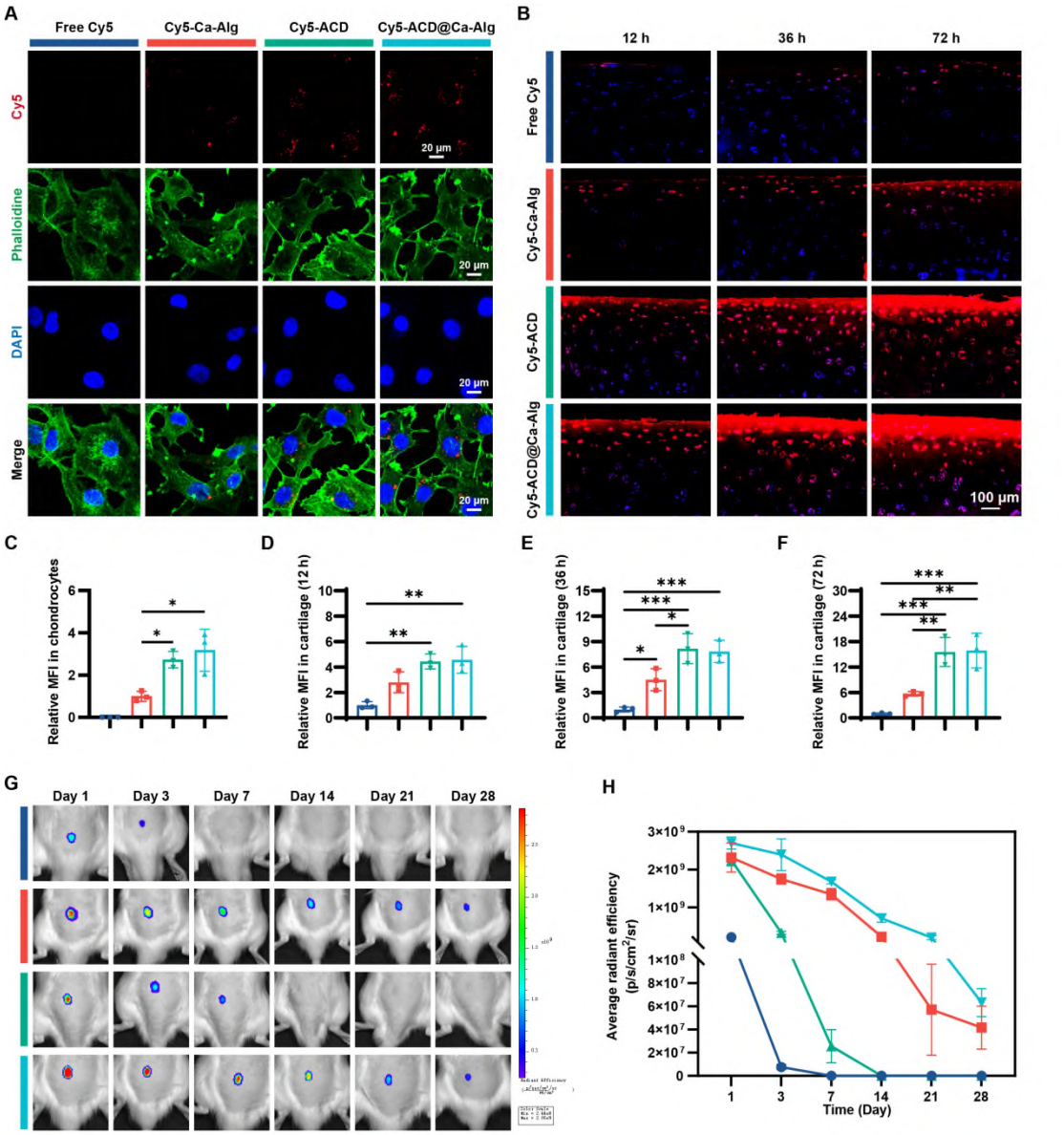


Figure 4. *In vitro* cellular uptake, *ex-vivo* deep-cartilage penetration behaviors, and *in vivo* retention of Cy5-labelled tracer formulations.

(A) Representative confocal microscopy images showing cellular internalization of Free Cy5, Cy5-Ca-Alg, Cy5-ACD and Cy5-ACD@Ca-Alg in primary chondrocytes. Red: Cy5-labelled tracer; green: phalloidin for F-actin cytoskeleton; blue:

DAPI-stained nuclei. Scale bar = 20 μm. (B) *Ex-vivo* penetration performance of different Cy5-labelled formulations in porcine cartilage explants after 12 h, 36 h and 72 h incubation. Red fluorescence represents tracer distribution inside cartilage tissue. Scale bar = 100 μm. (C) Quantitative analysis of relative intracellular Cy5 MFI in chondrocytes. (D-F) Quantification of relative intratissue MFI within cartilage at 12 h, 36 h and 72 h, respectively. (G) *In vivo* fluorescence imaging of lumbar facet joints at days 1, 3, 7, 14, 21, and 28 following local injection of different formulations. (H) Quantitative analysis of average radiant efficiency over 28 days, demonstrating sustained *in vivo* retention of Cy5-ACD@Ca-Alg. Data are presented as mean ± SD. *$p < 0.05$, **$p < 0.01$, ***$p < 0.001$. Cy5, Cyanine-5 fluorescent dye; MFI, mean fluorescence intensity; DAPI, 4′,6-diamidino-2-phenylindole.

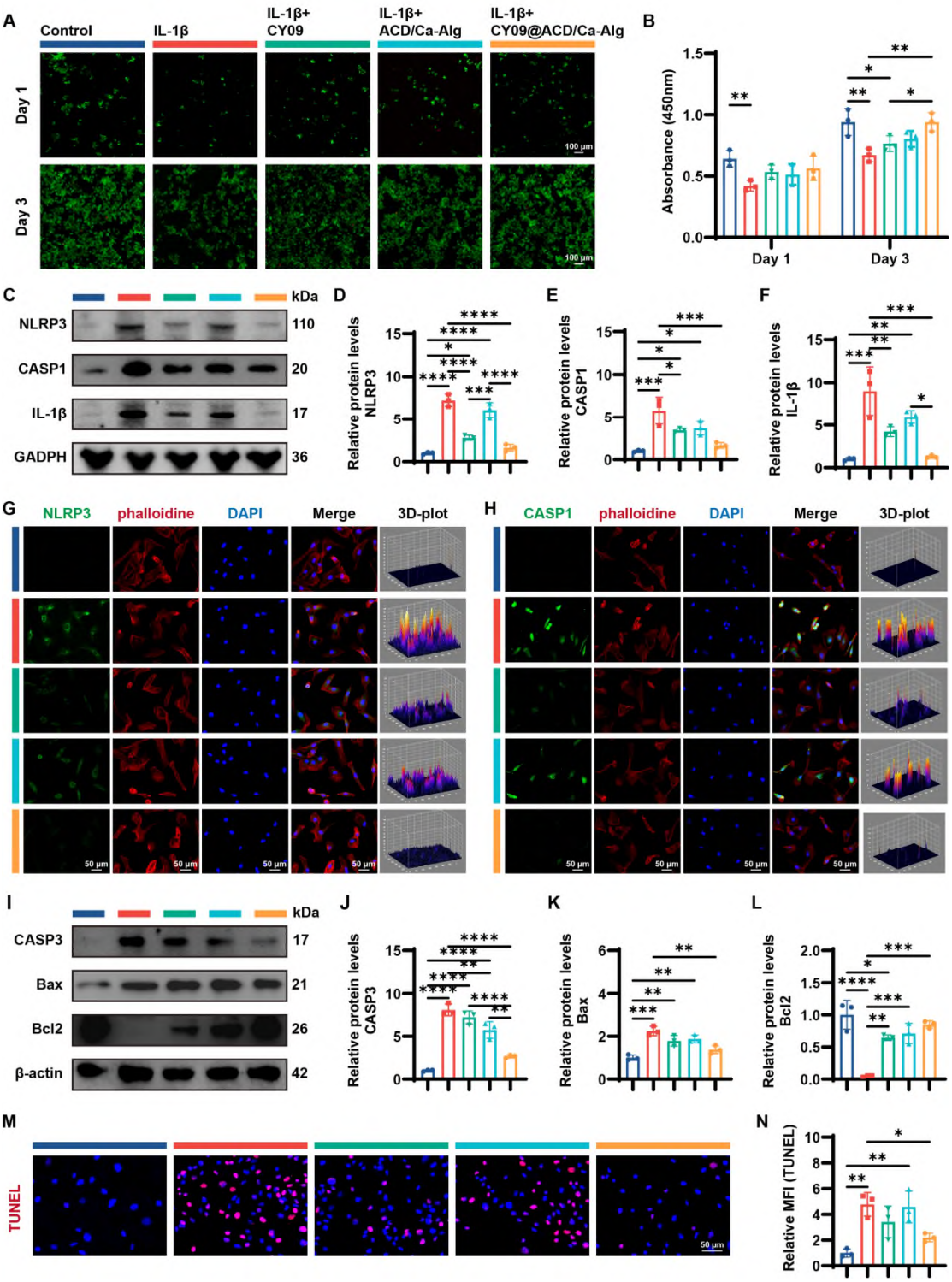


Figure 5. CY09@ACD/Ca-Alg hydrogel suppresses NLRP3-inflammasome activation and inhibits IL-1β-stimulated chondrocytes apoptosis.

(A) Live-dead fluorescence staining of chondrocytes from Control, IL-1β, IL-1β + CY09, IL-1β + ACD/Ca-Alg and IL-1β + CY09@ACD/Ca-Alg groups at

Day 1 and Day 3. Scale bar = 100 μm. (B) Quantitative absorbance-based viability statistics at Day 1 and Day 3. (C-F) Western-blot bands and quantitative analysis of NLRP3, caspase-1 and IL-1β protein expression across experimental groups. (G-H) Immunofluorescence staining and corresponding 3D-plot intensity visualization for NLRP3 and caspase-1. Scale bar = 50 μm. (I-L) Western-blot detection and quantification of apoptosis-associated markers caspase-3, Bax and Bcl-2. (M, N) TUNEL fluorescence staining and quantitative MFI analysis for inflammatory cell apoptosis. Scale bar = 50 μm. Data are presented as mean ± SD. *$p < 0.05$, **$p < 0.01$, ***$p < 0.001$, ****$p < 0.0001$. NLRP3, NOD-like receptor pyrin domain-containing-3; IL-1β, interleukin-1β; caspase-1, CASP1; GAPDH, glyceraldehyde-3-phosphate dehydrogenase; Bax, B-cell-associated X protein; Bcl-2, B-cell lymphoma-2; TUNEL, terminal deoxynucleotidyl transferase-mediated dUTP nick-end labelling; MFI, mean fluorescence intensity.

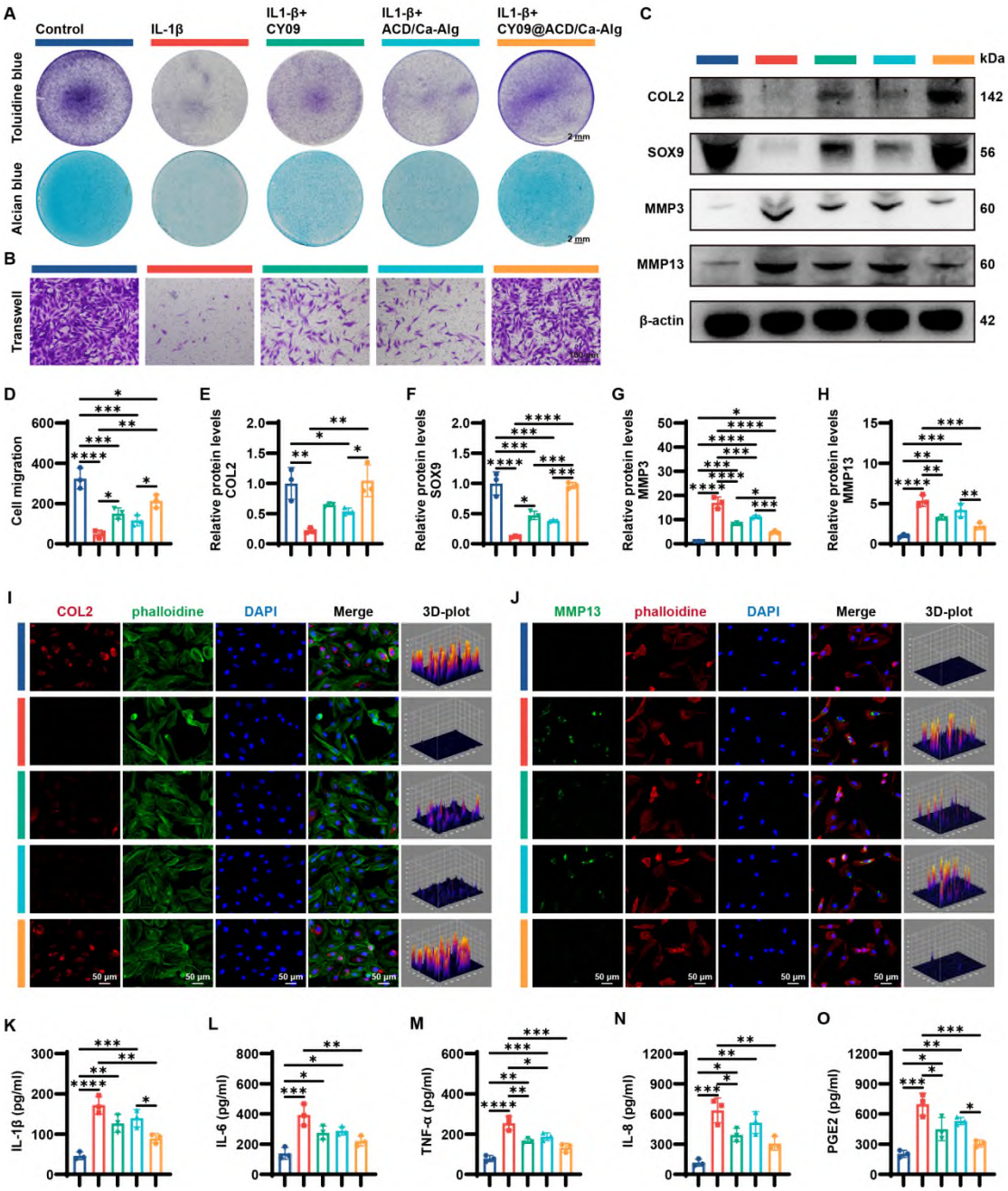


Figure 6. CY09@ACD/Ca-Alg hydrogel restores chondrocyte anabolic phenotype and reduces pro-inflammatory cytokine secretion under inflammatory stress.

(A) Toluidine-blue and Alcian-blue staining evaluating glycosaminoglycan synthesis of chondrocytes in different groups. Scale bar = 3 mm. (B, D) Transwell migration assay and quantitative cell-migration statistics. (C) Western-blot detection of chondrogenic (COL2, SOX9) and catabolic (MMP-3, MMP-13) protein markers.

(E-H) Quantitative analysis for relative protein levels of COL2, SOX9, MMP-3 and MMP-13. (I. J) Immunofluorescence staining and 3D-intensity-plot visualization for COL2 (red) and MMP-13 (green). Scale bar = 50 μm. (K-O) ELISA quantitative detection of pro-inflammatory cytokines IL-1β, IL-6, TNF-α, IL-8 and PGE2 in cell-culture supernatants. Data are presented as mean ± SD. *p < 0.05, **p < 0.01, ***p < 0.001, ****p < 0.0001. COL2, type-II collagen; TNF-α, tumor necrosis factor-α; MMP, matrix metalloproteinase; SOX9, SRY-box transcription factor 9; PGE2, prostaglandin E2; ELISA, enzyme-linked immunosorbent assay.

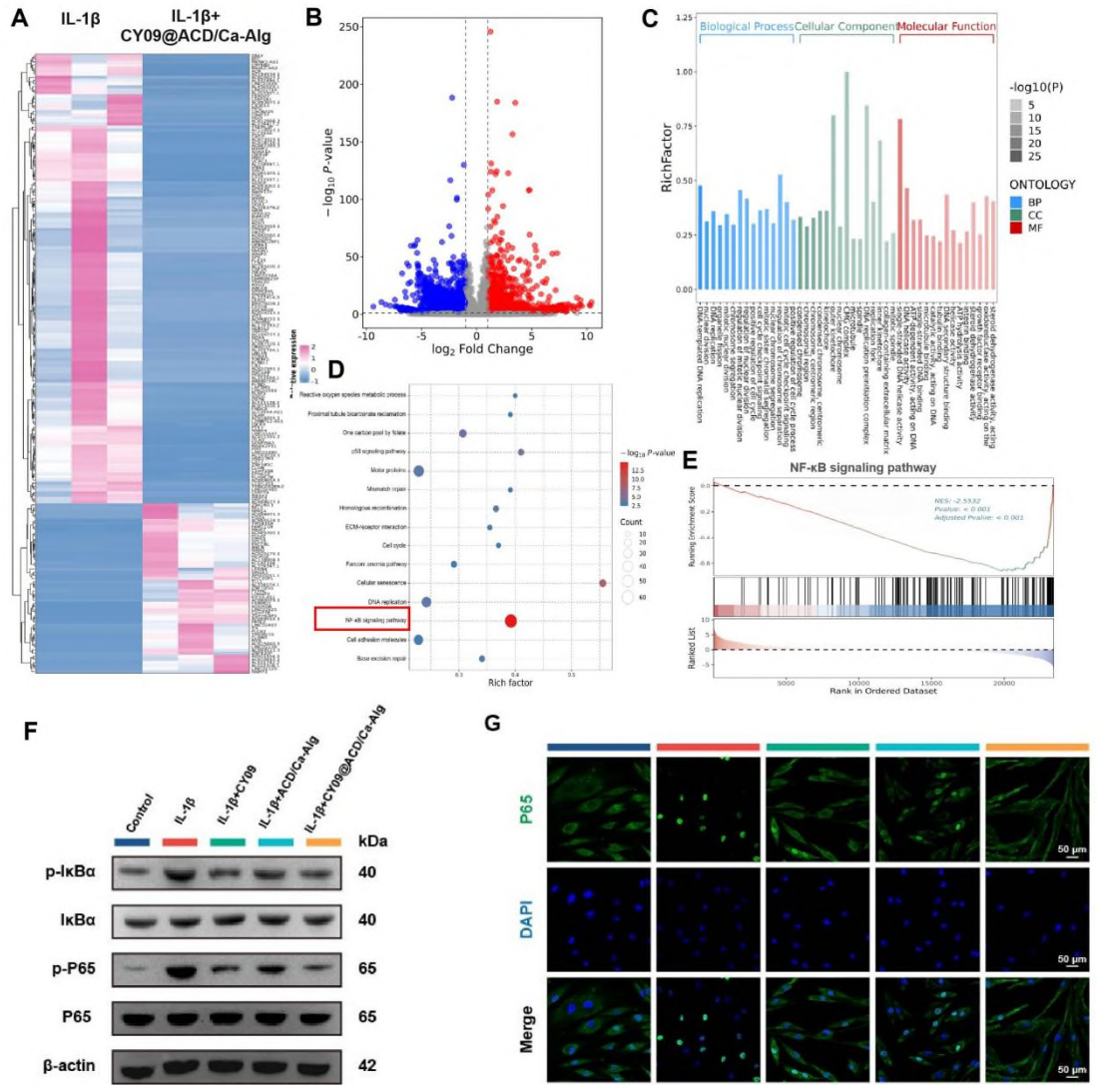


Figure 7. Transcriptomic RNA-sequencing identifies NF-κB signaling as core downstream mechanism of CY09@ACD/Ca-Alg-mediated chondro-protection.

(A) Heatmap showing distinct gene-expression profiles between IL-1β and IL-1β + CY09@ACD/Ca-Alg groups. (B) Volcano plot illustrating DEGs; red dots = significantly up-regulated genes, blue dots = significantly down-regulated genes. (C) Gene Ontology (GO) enrichment analysis covering biological process (BP), cellular component (CC), molecular function (MF). (D) KEGG-pathway bubble plot displaying top-ranked enriched signaling cascades. (E) GSEA plot showing significant negative enrichment of NF-κB-signaling-associated gene signature; NES, normalized enrichment score. (F) Western-blot detection of NF-κB-axis related proteins p-IκBα, IκBα, p-P65 and P65; β-actin as loading control. (G) Immunofluorescence staining for P65 (green) to evaluate P65 nuclear-translocation status; nuclei were counter-stained with DAPI (blue). Scale bar = 50 μm. Data are presented as mean ± SD. *$p < 0.05$, **$p < 0.01$, ***$p < 0.001$. DEG, differentially expressed gene; GO, Gene Ontology; KEGG, Kyoto Encyclopedia of Genes and Genomes; GSEA, Gene Set Enrichment Analysis; NES, normalized enrichment score; NF-κB, nuclear factor-κB; p-IκBα, phosphorylated inhibitor of nuclear factor-κB-α; p-P65, phosphorylated P65; DAPI, 4′,6-diamidino-2-phenylindole.

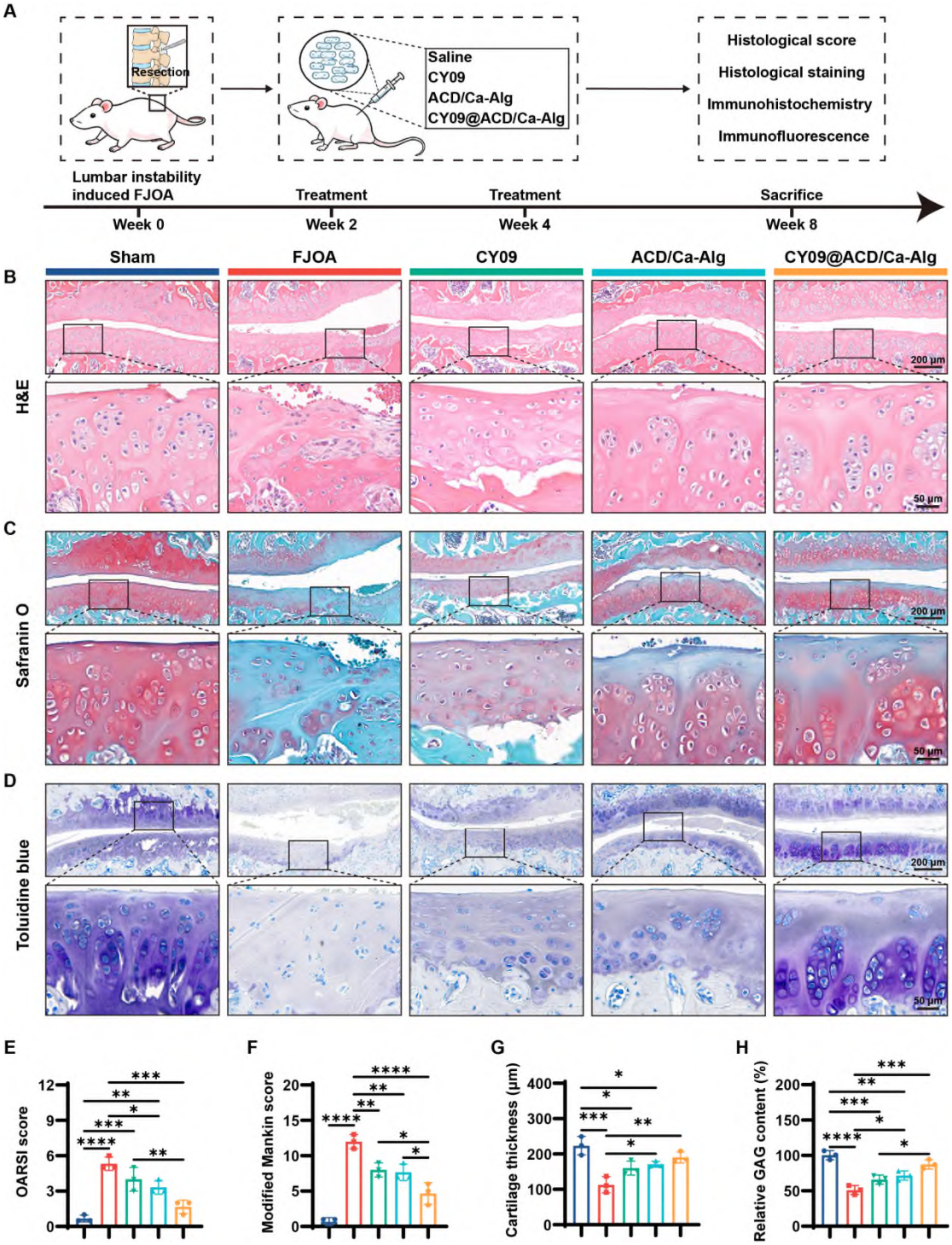


Figure 8. CY09@ACD/Ca-Alg hydrogel alleviates facet-joint degeneration in murine FJOA model.

(A) Schematic diagram of animal experimental grouping: Sham, FJOA, CY09, ACD/Ca-Alg, CY09@ACD/Ca-Alg. (B-D) Representative histological staining images: H&E, Safranin-O, Toluidine-blue for facet-joint cartilage from each group.

Scale bars: upper = 200 μm, lower = 50 μm. (E-H) Quantitative histological evaluation: OARSI score, modified Mankin score, residual cartilage thickness and relative GAG content. Data are presented as mean ± SD. *p < 0.05, **p < 0.01, ***p < 0.001, ****p < 0.0001. FJOA, facet-joint osteoarthritis; H&E, hematoxylin-eosin; GAG, glycosaminoglycan; OARSI, Osteoarthritis Research Society International.

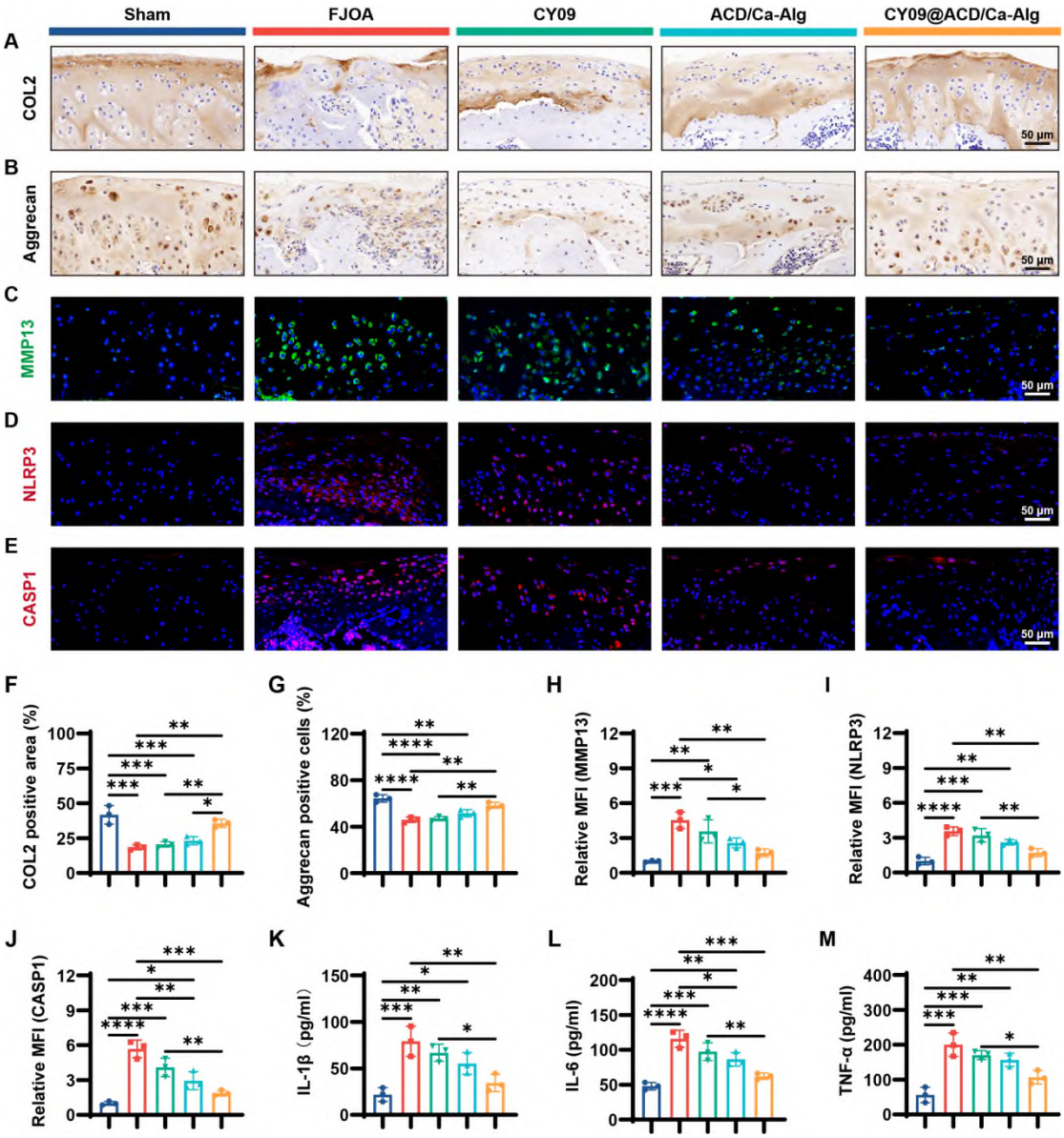


Figure 9. CY09@ACD/Ca-Alg preserves cartilage matrix and inhibits NLRP3-inflammasome-mediated inflammation *in-vivo*.

(A-B) Representative immunohistochemical staining of COL2 and Aggrecan in facet joint cartilage tissues. Scale bar = 50 μm. (C-E) Representative immunofluorescence

images of MMP13, NLRP3 and IL-1β in facet joint tissues. Nuclei were counter-stained with DAPI (blue). Scale bar = 50 μm. (F-G) Quantitative analysis of COL2- and Aggrecan-positive area percentage. (H-J) Quantification of relative mean fluorescence intensity (MFI) for MMP13, NLRP3 and IL-1β. (K-M) The concentrations of pro-inflammatory cytokines IL-1β, IL-6 and TNF-α in the joints determined by ELISA. Data are presented as mean ± SD. *$p < 0.05$, **$p < 0.01$, ***$p < 0.001$, ****$p < 0.0001$. COL2: Collagen type II, MMP13: matrix metalloproteinase, NLRP3: NOD-like receptor pyrin domain-containing protein 3, IL: interleukin, TNF: tumor necrosis factor, FJOA: facet joint osteoarthritis, ACD: cationic β-cyclodextrin, Ca-Alg: calciumalginate, GAG: glycosaminoglycan, MFI: mean fluorescence intensity.

Table 1: Characteristics of patients

Variable	Weishaupt grading system			
	Grade 0 (n = 8)	**Grade 1** (n=12)	**Grade 2** (n=15)	**Grade 3** (n=8)
Age (years)	25.9 ± 7.7	36.9 ±7.1	50.4 ± 5.9	69.4 ± 5.4
Men/Women	6/2	7/5	6/9	4/4
BMI	22.4 ± 3.3	24.1 ± 3.5	24.6 ± 4.6	24.4 ± 2.2
Diseases				
Spinal cord injury	8	0	0	0
Lumbar spinal stenosis	0	4	11	7
Lumbar disc herniation	0	8	4	1
Surgical level				
L1/2	6	0	0	0
L2/3	2	0	0	0
L3/4	0	1	1	0
L4/5	0	6	10	6
L5/S1	0	5	4	2

Data represent mean ± standard deviation. BMI, body mass index.

Supplementary Files

This is a list of supplementary files associated with this preprint. Click to download.

- Supplementalmaterial.docx
- Graphicabstract.tif
- FigureS1.tif